

Regional Differences in the Response of Rainfall to Convectively Coupled Kelvin Waves over Tropical Africa

LAWRENCE S. JACKSON,^a RICHARD J. KEANE,^{a,c} DECLAN L. FINNEY,^a JOHN H. MARSHAM,^{a,b}
DOUGLAS J. PARKER,^a CATHERINE A. SENIOR,^c AND RACHEL A. STRATTON^c

^a School of Earth and Environment, University of Leeds, Leeds, United Kingdom

^b National Centre for Atmospheric Science, School of Earth and Environment, University of Leeds, Leeds, United Kingdom

^c Met Office, Exeter, United Kingdom

(Manuscript received 7 January 2019, in final form 20 August 2019)

ABSTRACT


The representation of convection remains one of the most important sources of bias in global models, and evaluation methods are needed that show that models provide the correct mean state and variability, both for the correct reasons. Here we develop a novel approach for evaluating rainfall variability due to convectively coupled Kelvin waves (CCKWs) in this region. A phase cycle was defined for the CCKW cycle in OLR and used to composite rainfall anomalies. We characterize the observed (TRMM) rainfall response to CCKWs over tropical Africa in April and evaluate the performance of regional climate model (RCM) simulations: a parameterized convection simulation (P25) and the first pan-Africa convection-permitting simulation (CP4). TRMM mean rainfall is enhanced and suppressed by CCKW activity, and the occurrence of extreme rainfall and dry days is coupled with CCKW activity. Focusing on regional differences, we show for the first time that there is a dipole between West Africa and the Gulf of Guinea involving onshore/offshore shifts in rainfall, and the transition to enhanced rainfall over west equatorial Africa occurs one phase before the transition over east equatorial Africa. The global model used to drive the RCMs simulated CCKWs with mean amplitudes of 75%–82% of observations. The RCMs simulated coherent responses to the CCKWs and captured the large-scale spatial patterns and phase relationships in rainfall although the simulated rainfall response is weaker than observations and there are regional biases that are bigger away from the equator. P25 produced a closer match to TRMM mean rainfall anomalies than CP4 although the response in dry days was more closely simulated by CP4.

1. Introduction

The majority of rainfall over tropical Africa is associated with the tropical rain belt, a zone of heavy rainfall and deep convection that, in contrast to the oceanic intertropical convergence zone (ITCZ), is generally located equatorward of the maximum low-level wind convergence (Nicholson 2018). The rain belt migrates seasonally about the equator between the Northern and Southern Hemispheres with pronounced intraseasonal variations in rainfall (e.g., Nicholson 2013, 2017).

Convectively coupled Kelvin waves (CCKWs) are equatorially trapped envelopes of convection that travel

eastward at about $14\text{--}20\text{ m s}^{-1}$. CCKWs were originally regarded as super cloud clusters (SCCs; Nakazawa 1988). Wheeler and Kiladis (1999) showed that the family of equatorial modes predicted by the linear theory of Matsuno (1966) can be seen in normalized power spectra of satellite data such as outgoing longwave radiation (OLR). The significant overlay between the Matsuno curves and the OLR spectral peaks yielded the convectively coupled equatorial waves (CCEWs) definition. In particular, the SCCs associated with the theoretical, nondispersive Kelvin mode were regarded as CCKWs. Recently, Blanco et al. (2016) proposed a decoupling mechanism for idealized CCKWs (simulated under zonally homogeneous

 Denotes content that is immediately available upon publication as open access.

Corresponding author: Lawrence S. Jackson, l.s.jackson@leeds.ac.uk



This article is licensed under a Creative Commons Attribution 4.0 license (<http://creativecommons.org/licenses/by/4.0/>).

conditions) in which the SCCs originate and dissipate but the dynamical (Kelvin) component remains mostly unchanged.

Observed CCKWs have a zonal pattern of alternating high and low surface pressure anomalies accompanied by alternating cloud brightness temperature (CBT), OLR, and precipitation anomalies. They are initiated by diabatic heating events at the equator (e.g., deep convection) and by extratropical forcing (Straub and Kiladis 2003a; Yang et al. 2007; Kiladis et al. 2009; Liebmann et al. 2009). Variations in cloudiness are maximized at latitudes where the CCKWs interact with the tropical rain belt (Roundy and Frank 2004).

The dynamical structures of observed CCKWs are similar to the equivalent theoretical solution in Matsuno's 1966 shallow water theory (Matsuno 1966; Kiladis et al. 2009). In the lower troposphere (~ 850 hPa) there is zonal wind convergence associated with westerly anomalies to the west of the minimum in CBT and easterly anomalies to the east with the maximum wind convergence approximately 1/8th of a cycle to the east of the minimum in CBT (Straub and Kiladis 2003b). In the upper troposphere (~ 200 hPa), the wind anomalies are broadly reversed and there is wind divergence that includes a meridional mass flux component (Kiladis et al. 2009). The maximum in upper-level wind divergence is collocated with the minimum in CBT indicating that the CCKWs have a tilted vertical structure (e.g., Straub and Kiladis 2003b). The most intense anomalies in ascending motion are collocated with the minimum in CBT and anomalies in downward motion are mainly located to the east of the minimum in CBT (Straub and Kiladis 2003b). Note, however, that CBT and OLR may also lag deep convection due to the tendency of cirrus cloud to persist after convection (Roundy and Frank 2004).

Although many authors have proposed that the Madden-Julian oscillation (MJO) and CCKWs are two distinctive phenomena in terms of signals in frequency-wavenumber space, horizontal structure, and dynamics, Roundy (2012, 2014) has suggested that both tropical modes are part of a continuum of disturbances propagating eastward over a wide range of phase speeds. As a matter of fact, it has been documented that many CCKWs circumnavigate the globe with varying velocity and intensity depending on the region of Earth, sometimes even as fast, dry Kelvin waves, and once they enter the warm pool region, they slow down, transitioning into (rather than "triggering") MJO events. In turn, these envelopes of convection typically speed up after crossing the Maritime Continent into the western Pacific, taking again the characteristics of CCKWs (Matthews 2008; Haertel et al. 2015).

The passage of CCKWs over tropical Africa has been detected in satellite retrievals of CBT and OLR, and CCKWs are associated with more variance in CBT over tropical Africa than other types of tropical modes (Laing et al. 2011). Further, the effects of CCKWs have been detected in Tropical Rainfall Measuring Mission (TRMM) rainfall data (3B42) and in reanalyses (Mekonnen et al. 2006; Mounier et al. 2007; Wang and Fu 2007; Mekonnen et al. 2008). These studies, the first to focus specifically on tropical Africa, detected CCKWs with phase speeds of ~ 15 m s⁻¹ and periods centered on 6–7.5 days during the boreal spring and summer seasons. CCKWs exhibit a strong seasonal cycle in activity and are most frequent in March–May and least frequent in September–November (Laing et al. 2011).

CCKWs contribute to variability in rainfall through phases of enhanced and suppressed convection detected throughout tropical Africa including West Africa (e.g., Mounier et al. 2007; Janicot et al. 2009; Mera et al. 2014; Schlueter et al. 2019a), equatorial Africa (e.g., Nguyen and Duvel 2008; Laing et al. 2011; Kamsu-Tamo et al. 2014; Sinclair et al. 2015), and East Africa (e.g., Mekonnen and Thorncroft 2016). The impact of CCKWs on rainfall is, however, greatest north of the equator due to the mean location of the tropical rain belt also being north of the equator (Mekonnen et al. 2008).

Also, CCKWs modulate the life cycle and track of mesoscale convective systems (MCS; Mounier et al. 2007). During the enhanced convection phase of CCKWs, MCSs in Africa are larger and more intense (Nguyen and Duvel 2008; Laing et al. 2011). Taylor et al. (2017) show that increased wind shear drives more intense convection in MCSs over the Sahel region and Schlueter et al. (2019b) show that increased wind shear is closely associated with the wet phase of CCKWs during the West African monsoon (WAM). Further, Sinclair et al. (2015) found strengthened midlevel easterlies and changes in vertical wind shear were prevalent during the active phase of CCKWs over the Congo basin and at storm scale, the propagation of convection over this region is associated with shear between low-level southwesterlies and the midlevel easterly jet (Laing et al. 2011). Different dynamical processes drive the regional responses of east and west equatorial Africa (e.g., Sandjon et al. 2014), and it is possible that rain bearing systems over east equatorial Africa are suppressed, rather than enhanced, by shear.

General circulation models (GCMs) commonly display pronounced biases in simulating CCKWs. In a study of CMIP3 climate models, Huang et al. (2013) found only 2 of 10 GCMs simulated CCKW activity in the expected latitudinal band near the equator [both were variants of the Japan Center for Climate System

Research (JP_CCSR3.2) model] and only 2 models produced a realistic seasonal cycle for CCKW activity. In a study of CMIP5 models, Wang and Li (2017) found bias in the latitudinal position of CCKW activity over the Pacific Ocean to be common among the GCMs. They also concluded that bias in simulated CCKWs was associated with bias in the mean state of precipitation. In a study of subseasonal forecasts of CCKWs and the MJO, Janiga et al. (2018) found all three of their chosen GCMs simulated less CCKW activity than in OLR observations. Simulated CCKWs are sensitive to the representation of moist convection in GCMs. For example, changing the strength of convective triggers in models to make it more difficult for deep convection to occur yields slower and more intense simulated CCKWs (Frierson et al. 2011). Additionally, in GCMs with convective parameterizations using adjustment-based closure schemes, more realistic CCKW activity was achieved by the inclusion of a convective trigger function that acted to suppress deep convection and facilitate the buildup of low-level moisture ahead of the CCKWs (Straub et al. 2010; Huang et al. 2013).

While these earlier studies have shed light on the role of CCKWs in modulating African rainfall, the broader continental perspective is still lacking. For example, studies of the MJO over the Maritime Continent region have shown how the response of rainfall to the wave forcing is significantly different over land and sea (Birch et al. 2016): Are there comparable regional differences in CCKW coupling over Africa?

Furthermore, model performance in representing the rainfall responses to CCKW forcing is still unclear. Large-scale analysis of the response of rainfall to CCKWs tests convection schemes beyond the mean climate state. It tests that the convection is coupling correctly with the varying environment taking account of intraseasonal variability. Recent studies using convection-permitting models have shown improvements compared to models with parameterized convection in simulations of deep convection and extreme rainfall and over mountainous regions (Prein et al. 2015): Will this improve the response of a model to dynamical forcing from a CCKW over tropical Africa?

The aims of this study, therefore, are to advance understanding of the role of CCKWs in the variability of rainfall across tropical Africa and test the performance of climate models simulating this variability. We focus on the April rainfall, a month of high seasonal rainfall over west and east tropical Africa (e.g., Washington et al. 2013; Nicholson 2017, respectively) and a precursor to the WAM in its coastal phase (May–June) and over the Sahel (July–September) (Nicholson and Grist 2003). More specifically, our objectives are as follows:

- Investigate the influence of CCKWs on the spatiotemporal patterns of rainfall variability in observations over tropical Africa;
- compare the performance of two RCM simulations, one with parameterized convection and the other with explicit convection; and
- provide results to support the future development and evaluation of GCMs.

In section 2 we describe the model simulations, data, and methodology used to divide the cycle of CCKW-filtered OLR anomalies into phases for comparing rainfall and dynamical relationships. Section 3 describes the results, and section 4 presents our discussion and conclusions.

2. Climate model, data, and methodology

a. Regional climate model configurations

Two RCM configurations were run independently for a limited area domain (Stratton et al. 2018). The domain extended from 45°S to 40°N and from 25°W to 56°E to include the whole of Africa and locate the boundaries away from the coast of Africa. Both RCM configurations used the Met Office Unified Model (UM), which is a nonhydrostatic model with a semi-implicit, semi-Lagrangian dynamical core. Both configurations were based on Even Newer Dynamics for General Atmospheric Modeling of the Environment (ENDGame) dynamics (Wood et al. 2014). Lateral boundary conditions for both configurations were driven by one-way nesting (Davies 2014) in an unnudged global N512 AMIP simulation with 85 vertical levels using the Global Atmosphere/Land 7.0 (GA7/GL7) configuration of the UM (Walters et al. 2019), herein referred to as G25. The G25 and RCM simulations were forced with sea surface temperatures (SST) derived from the Reynolds dataset of daily high-resolution blended analyses for SST on a regular spatial grid of 0.25° resolution (Reynolds et al. 2007). The G25 simulation was run for years 1988–2010.

The RCM simulations were run for 10 years (1997–2006). Atmospheric greenhouse gas (GHG) concentrations had fixed global values that were updated annually. Aerosol concentrations in the RCMs were based on climatologies from an earlier version of the climate model that used the Coupled Large-Scale Aerosol Simulator for Studies in Climate (CLASSIC) aerosol scheme (Walters et al. 2019). Aerosols in the G25 model were interactive and used the UK Chemistry and Aerosols (UKCA) scheme. The RCM simulations used GHG concentrations based on those for the G25 simulation and interpolated to their regional model grids.

The initial conditions for the RCM atmospheres were taken from the G25 simulation at 1 January 1997. For further details of the G25 and RCM simulations, including tables that list the differences between the RCM simulations, see [Stratton et al. \(2018\)](#).

In our analysis of the RCM simulations, 10 years' data at hourly frequency were used for rainfall. Data for the pressure level diagnostics were 3 hourly and available for 9 years (1998–2006); the CP4 pressure level diagnostics were not archived for the first 6 months of 1997 due to a problem with the model setup.

1) PARAMETERIZED CONVECTION SIMULATION (P25)

The parameterized convection RCM configuration used a horizontal grid resolution of ~ 25 km latitude and ~ 39 km longitude at the equator, the same as the G25 simulation, and 63 vertical levels up to 41 km. Parameterized convection was based on the Gregory–Rowntree mass flux scheme ([Gregory and Rowntree 1990](#)) with several enhancements including, for example, allowance for downdrafts, convective momentum transport, and a closure based on convectively available potential energy ([Walters et al. 2017](#)). The prognostic cloud scheme PC2 ([Wilson et al. 2008](#)) was used in the P25 configuration (and also in the G25 simulation).

2) CONVECTION-PERMITTING SIMULATION (CP4)

The convection-permitting RCM configuration used a horizontal grid resolution of ~ 4.5 km latitude and longitude at the equator and 80 vertical levels up to 38.5 km. Convection was represented explicitly using the model dynamics although it only partly resolved deep convection on a 4.5-km grid resolution and cannot resolve smaller-scale congestus or shallow convection ([Stratton et al. 2018](#)). Previous studies, however, in which the convection parameterization was removed from the UM at this resolution yielded an improved spatial distribution of rainfall and an improved diurnal cycle compared to TRMM ([Birch et al. 2014](#)).

In addition to differences in model resolution and the representation of convection, there are other notable differences between the P25 and CP4 simulations. The large-scale cloud scheme used in CP4 is described by [Smith \(1990\)](#) and has been used in previous convection-permitting versions of the UM. Following [Lock et al. \(2000\)](#), CP4 included stochastic perturbations in the subcloud layer of cumulus-capped boundary layers to improve the triggering of resolved convection.

To facilitate comparison of the CP4 and P25 simulations, data from the CP4 simulation were regridded using area weighting to the P25 horizontal grid resolution. To compare the two simulations on a scale in which

convection is expected to be resolved, maps are presented at 150-km resolution (i.e., 6 times the P25 resolution).

b. Observations

National Oceanic and Atmospheric Administration (NOAA) interpolated OLR ([Liebmann and Smith 1996](#); [NOAA 2018](#)) was used to detect CCKW anomalies. Daily mean interpolated OLR data at the top of atmosphere from 1998 to 2007 (inclusive) were used with a global grid resolution of 1° latitude \times 1° longitude. The data were downloaded from the website at <https://www.esrl.noaa.gov/psd/>.

The TRMM Multisatellite Precipitation Analysis 3B42, version 7, rainfall dataset was used for observations of rainfall ([Huffman et al. 2007](#); [NASA 2015](#)). The 3B42 rainfall is based on rainfall estimates from multiple satellites combined with bias correction using monthly land surface rain gauge data. Daily mean rainfall was derived from 3-hourly observations of rainfall from 1998 to 2007 (inclusive) on a regular grid resolution of 0.25° . The data were regridded from the TRMM grid to the P25 model grid for ease of comparison with data from the P25 and CP4 simulations. The April monthly means were calculated over the 10 years from 1998 to 2007.

c. Calculation of CCKW-filtered OLR anomaly time series

Observed daily mean OLR was averaged between 15°N and 15°S for circumequatorial longitudes over the 10 years' data, and a spectral analysis was performed on this longitude–time space. [Frierson et al. 2011](#) note that this approach slightly emphasizes CCKW variability over other wave modes compared to the [Wheeler and Kiladis \(1999\)](#) method. The spectral analysis was applied to 96-day segments of the time series separated by a gap of 15 days between segments. The CCKW-filtered OLR anomalies were produced by filtering the latitudinally averaged OLR fields in longitude and time. A space–time Fourier transform was taken followed by an inverse Fourier transform on only those parts of the spectrum corresponding to Kelvin waves. We used a wavenumber range of 0–15, a frequency range of 2–90 cycles per day, and an equivalent depth range of 12–90 m to produce a Kelvin wave–filtered OLR anomaly field varying in longitude and time (polygons in [Figs. 1a–d](#)). We followed [Wheeler and Kiladis \(1999\)](#) in setting these parameters with one exception: we used an equivalent depth of 12 m instead of 8 m. The same procedure was used for the observed and the simulated OLR.

[Figures 1a and 1b](#) show the raw zonal wavenumber–frequency power spectra (i.e., before normalization) for NOAA OLR and the G25 simulation. The normalized

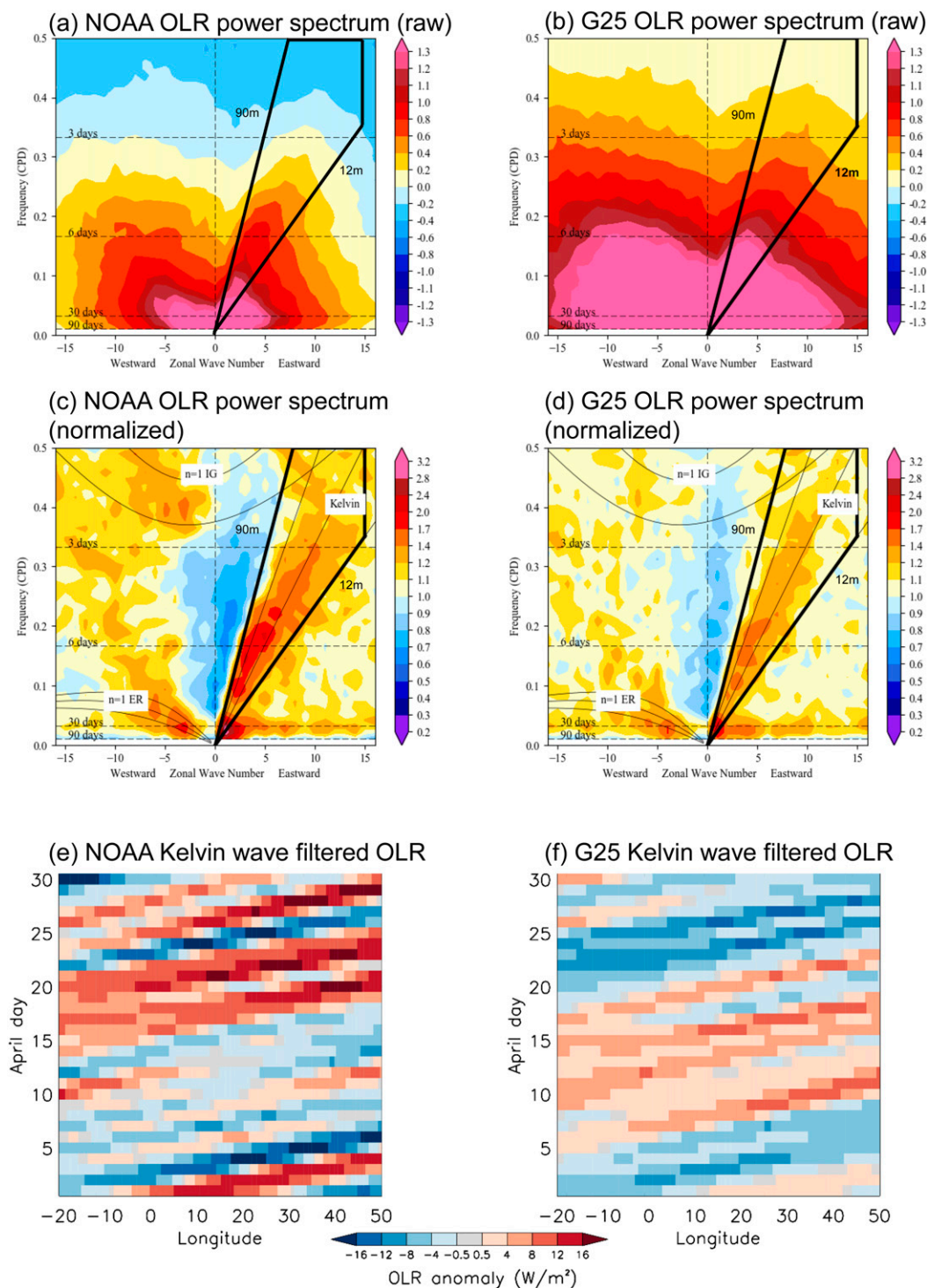


FIG. 1. (a) NOAA OLR raw power spectrum (base 10 logarithm), symmetric about the equator and averaged over latitudes $15^{\circ}S$ – $15^{\circ}N$. (b) As in (a), but for the G25 simulation. (c) As in (a), but normalized by dividing by the background spectrum. (d) As in (b), but normalized. In (a)–(d), the theoretical dispersion curves for equatorial waves are represented by the overlaid black lines and the region filtered for Kelvin waves is bounded by the polygon in bold. (e) April 1997 Hovmöller for the NOAA Kelvin wave-filtered OLR. (f) As in (e), but for the G25 simulation.

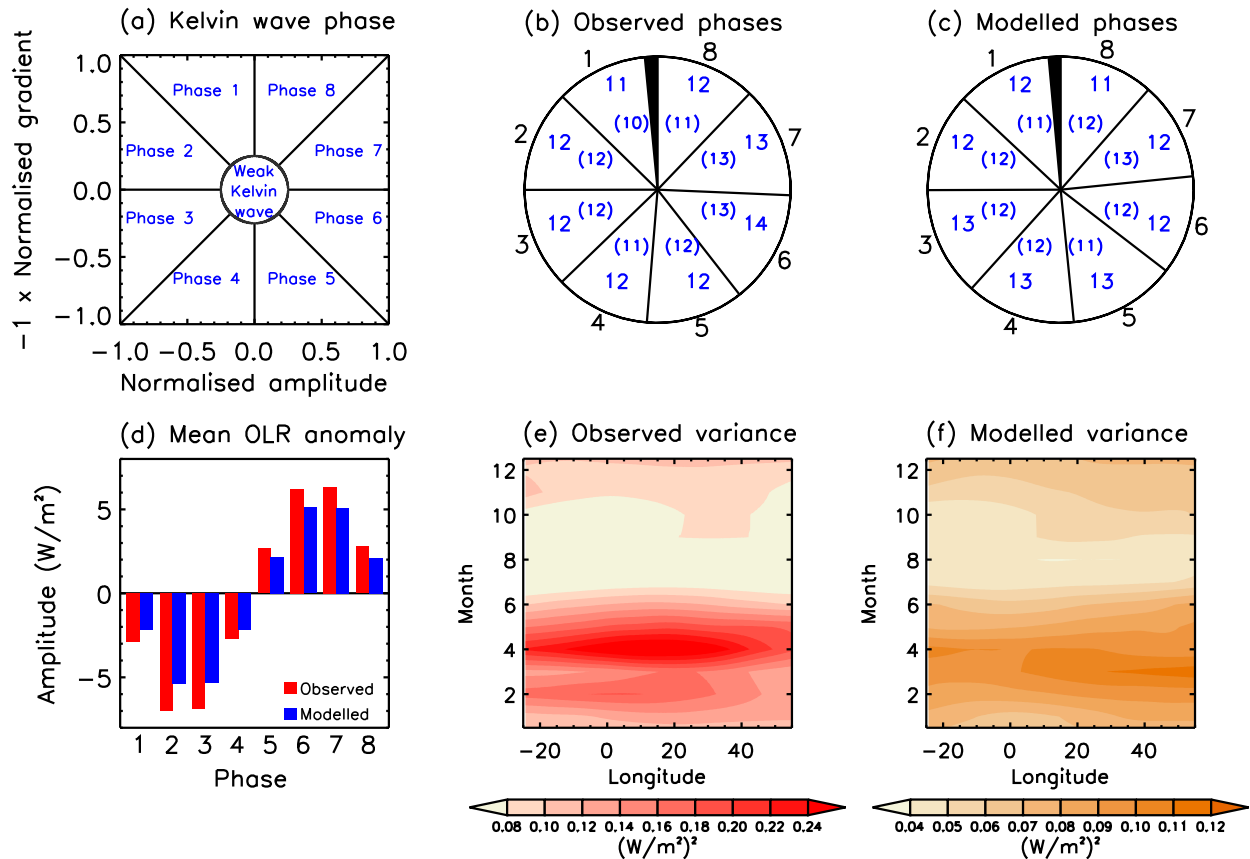


FIG. 2. (a) Kelvin wave phase defined from the normalized filtered OLR amplitude and gradient. (b) Pie chart showing the percentage of days allocated to each phase in April with the equivalent percentages for annual data quoted in parentheses. The days of weak Kelvin wave activity (which were discarded from the analysis) are represented by the shaded segment. (c) As in (b), but for the G25 simulation. (d) Mean filtered OLR anomaly split by the Kelvin wave phase for NOAA OLR observations and the GL simulation. (e) Monthly variance by longitude of Kelvin wave–filtered OLR anomalies for the NOAA observations. (f) As in (e), but for the G25 simulation.

zonal wavenumber–frequency power spectra (Figs. 1c,d) show that the zonal wavenumber–frequency power spectrum for the G25 simulation has a similar structure to the observed OLR. It has spectral peaks for CCKWs concentrated between periods of 3 and 30 days and a peak intensity centered on 6 days. Figures 1e and 1f show specimen Hovmöller diagrams for CCKW-filtered OLR anomalies during April 1997. The G25 simulation captures the eastward-propagating waves and the similarity of the OLR anomaly gradients in G25 and observations indicates that the phase speeds are broadly consistent with observations. The amplitude of the OLR anomalies in G25, however, is markedly weaker than in observations.

d. Definition of CCKW phases

To investigate the relationships between the CCKW OLR anomalies and rainfall, eight phases were defined for the CCKWs based on the OLR anomaly amplitude and gradient (Fig. 2a). The phase boundaries shown in

Fig. 2a were adopted because they are effective at discriminating rainfall maxima and minima. Using eight phases provided more effective discrimination between mean rainfall amounts by phase compared with using a smaller number of phases, for example, four phases as used by Nguyen and Duvel (2008). To ensure that the allocation of days to each phase was not prejudiced by differences in units and the range of data between the OLR amplitude and gradient, the OLR anomaly data were normalized before the phase was determined. Normalization involved subtraction of the mean value and division by the standard deviation with the mean and standard deviation calculated over the same 10-yr period as the OLR anomaly data. To strengthen the signal in the data over noise, data points with relatively weak amplitudes and gradients were excluded from the data allocated to phase, that is, where $\sqrt{(a^2 + g^2)} < 0.25$, where a represents the normalized amplitude and g represents the normalized gradient.

The CCKW phases and associated rainfall anomalies were calculated for each grid cell using the local (nearest longitude) CCKW OLR anomaly based on the NOAA OLR data for TRMM rainfall and the G25 simulated OLR for the P25 and CP4 simulations. The OLR anomalies from the G25 simulation were used to define the CCKW activity for the P25 and CP4 simulations because, as well as providing the lateral boundary conditions for both P25 and CP4, G25 simulated OLR over a global equatorial domain equivalent to that available for the NOAA OLR data.

3. Results

a. CCKW OLR anomalies

In this section, the CCKW-filtered OLR anomalies for the G25 simulation are compared with observations. The percentage allocation of days to the CCKW phases is shown in Figs. 2b and 2c. The days are broadly evenly distributed between the eight phases, both for the observed data and for the G25 simulation. For the observations, 2% of the days are discarded from April data and 6% from annual data and, for the G25 simulation, 2% and 5% of the days are discarded, respectively. The mean OLR anomaly for each phase is shown in Fig. 2d. The CCKW anomalies in the G25 simulation are weaker than the anomalies in the observations, varying between 75% and 82% of the observed mean in each phase—a result that is in agreement with the OLR anomalies shown in Figs. 1e and 1f. In Fig. 2d, phases 6 and 7 share the maximum OLR anomalies and the minimum OLR anomalies are shared between phases 2 and 3.

To show the magnitude of variation in OLR about its mean state caused by CCKWs, the monthly mean variance in observed OLR anomalies is plotted in Fig. 2e. The largest variances occur in January–June with the maximum variance in April (which is why we focus on the month of April in this study). The variance decreases sharply to a minimum in August before increasing gradually during September–February. The seasonal cycle of the OLR anomaly variance in G25 (Fig. 2f) varies over a narrower range of values than the observations. Further, the seasonal cycles differ in that the maximum variance in G25 occurs in March, rather than April, and this may contribute toward the smaller April OLR anomalies in G25. In contrast to the observations, the variance in G25 is greater over East Africa than farther west. This geographic variation is small, however, relative to the overall difference in variance between G25 and the observations (Figs. 2e,f).

b. Mean climate for rainfall

During April, the rain belt is located over the equator, which contributes to the strongest seasonal interactions between CCKW dynamics and convection (Figs. 2e,f). In TRMM rainfall (Fig. 3a), as the rain belt migrates northward across tropical Africa, there is particularly high rainfall over the Gulf of Guinea (GoG) and the eastern equatorial Atlantic Ocean, the west coast of equatorial Africa (\sim equator), the eastern boundary of the Congo basin (\sim 25°E), Lake Victoria, and the east coast of Africa (\sim 6°S). The variance in TRMM daily mean rainfall (Fig. 3b) includes days of no rain as well as wet days and includes variation in rainfall from all causes. The TRMM rainfall variance is large in regions of high rainfall. The variance is also large over the Congo basin likely associated with the westward-propagating storms initiated over the Rwenzori and Virunga Mountains located along the eastern boundary of the Congo basin (Laing et al. 2011), and the high frequency of intense storms over the region (Zipser et al. 2006).

The differences in mean April rainfall between TRMM and the P25 and CP4 simulations are shown in Figs. 3c and 3e. CP4 has a smaller bias in its large-scale rainfall than P25 (Stratton et al. 2018) although both simulations have in common significant regional biases. The simulations have too much rainfall over land and particularly over mountains. Both simulations have too little rainfall over the west coast of equatorial Africa. Over the east coast of Africa at \sim 6°S, P25 has too much rain, whereas CP4 has too little. Over the GoG, CP4 performs well, whereas P25 has a large dry bias. These regional biases will be due, in part, to biases in the positioning of the rain belt as well as biases in local rainfall frequency, intensity, and duration. For example, the dipole in rainfall bias in P25 over the eastern equatorial Atlantic is likely due to the simulated rain belt being farther south than in TRMM. The differences in April rainfall variance between TRMM and the P25 and CP4 simulations are shown in Figs. 3d and 3f. Where rainfall in P25 and CP4 is lighter than TRMM the variance is smaller than TRMM. The rainfall variance is also smaller than TRMM, however, over the Congo basin, and parts of East Africa and the GoG where rainfall is more intense in P25 and CP4.

Further evaluation of the P25 and CP4 simulations is available in Stratton et al. (2018), in Berthou et al. (2019) for West Africa and in Finney et al. (2019) for East Africa.

c. The CCKW component of mean rainfall

The proportion of variance in meridional mean rainfall (15°S–15°N) explained by CCKW activity is shown

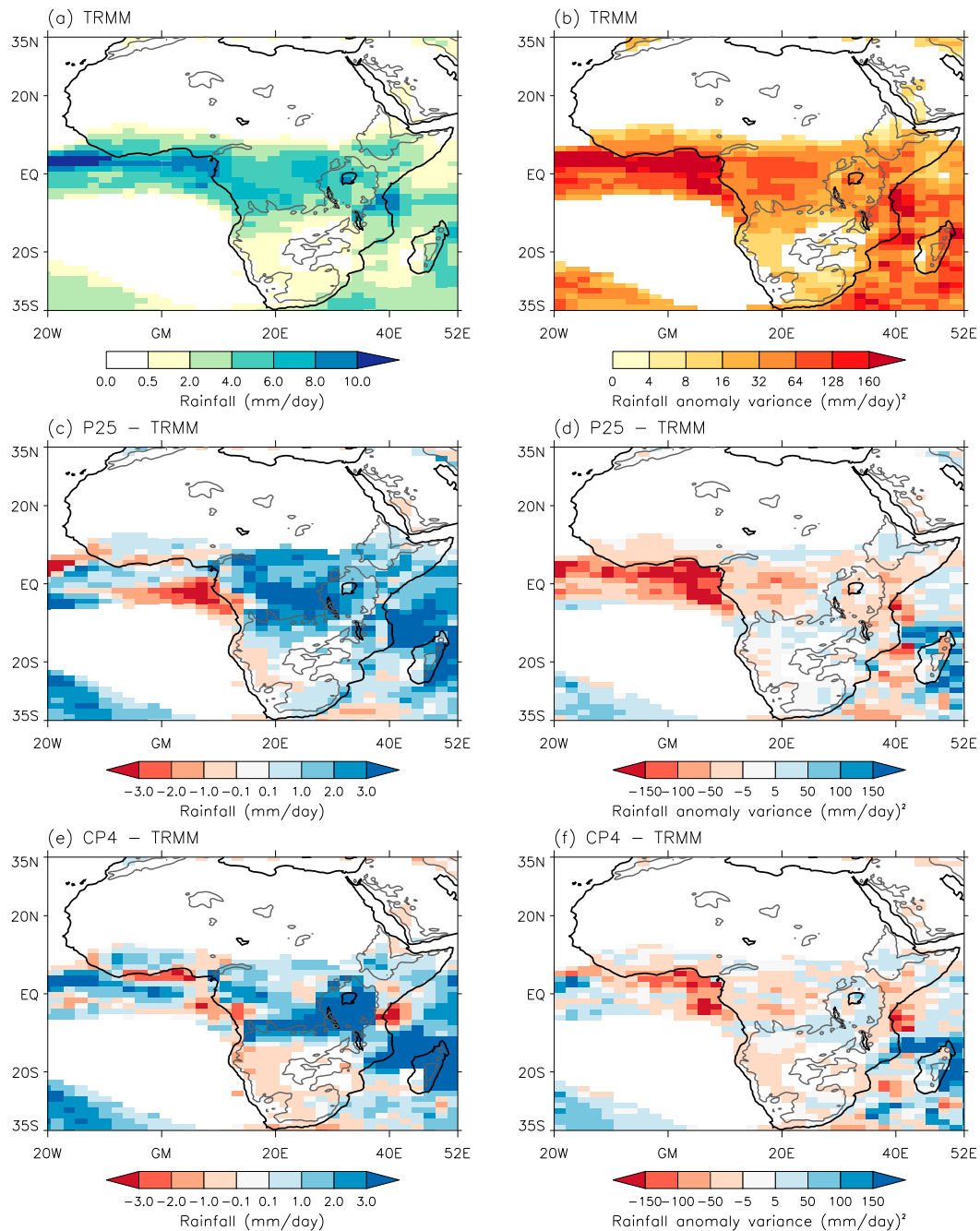


FIG. 3. (a) April monthly mean rainfall from TRMM averaged over years 1998–2007, (c) the difference between April monthly mean rainfall from the P25 simulation (1997–2006) and TRMM, and (e) as in (c), but for the CP4 simulation. (b) The variance in daily mean rainfall during April after the removal of interannual variability for TRMM, (d) the difference in variance between the P25 simulation and TRMM for April, and (f) as in (d), but for the CP4 simulation. The gray contour lines show the orography at 1000-m elevation. The data are plotted at 150-km resolution.

in Fig. 4. For TRMM rainfall, CCKWs account for ~15% of rainfall variance over West Africa, the GoG, equatorial Africa, much of East Africa, and less than 5% over the Horn of Africa and the western Indian Ocean.

The CP4 and P25 simulations underestimate the proportion of rainfall variance attributed to CCKWs. In the P25 simulation over equatorial Africa (15°–35°E); however, the proportion of rainfall variance explained

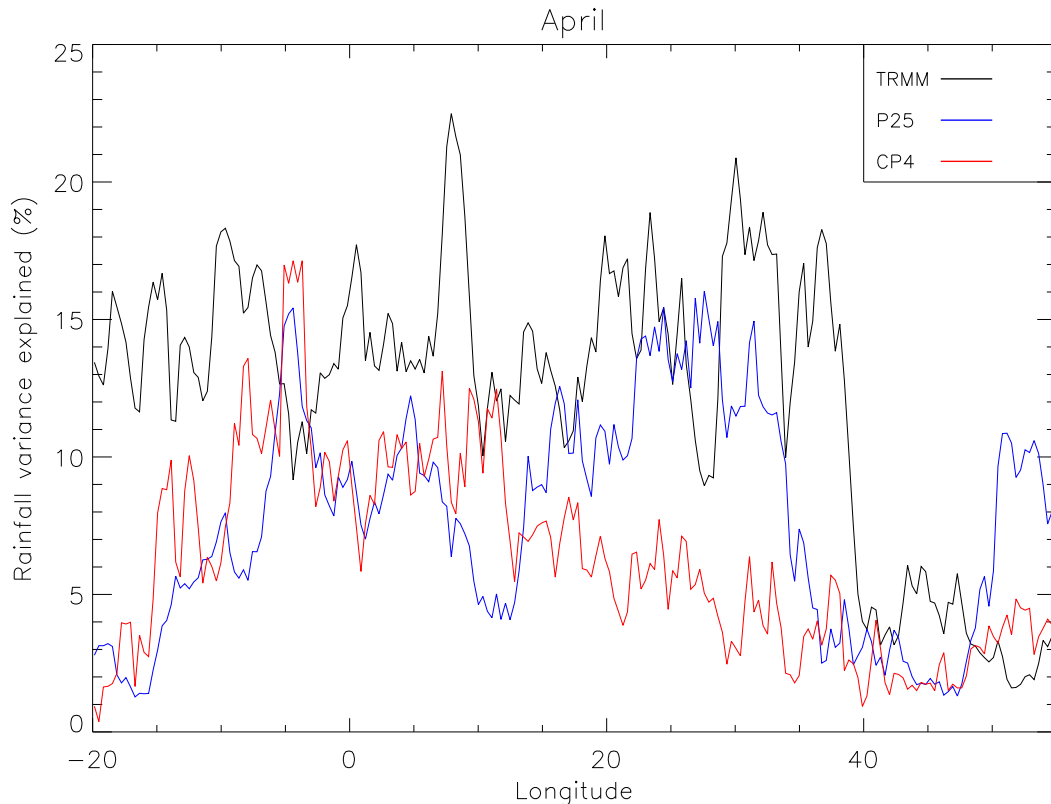


FIG. 4. The proportion of variance in April daily mean rainfall explained by Kelvin wave activity. Rainfall was averaged over latitudes 15°S–15°N, and interannual variability in April rainfall was filtered out before the variance explained was calculated.

by CCKW activity is greater than in the CP4 simulation and closer to the proportion explained in TRMM rainfall.

The anomalies in mean April rainfall in TRMM (Fig. 5) reveal large-scale spatial patterns with clusters of positive and negative anomalies that vary coherently by CCKW activity. The anomalies are smaller away from the equator (Fig. 5, boxes B, C, D, G, and H) reflecting the lighter rainfall (Fig. 3a) and the diminishing amplitude of CCKWs with greater distance from the equator. A bootstrap resampling of the meridional mean rainfall anomalies by CCKW phase showed that they were significantly different from zero at the 1% significance level.

The distribution of rainfall anomalies shows remarkable spatial variability across the continent, which is apparent in the presence of regions of coherent positive or negative rainfall anomaly in every wave phase and is particularly strong in the transitional phases. Broadly speaking, the rainfall distribution over the GoG (Fig. 5, box A, 10°W–5°E, 5°S–5°N) follows the cycle expected from the OLR pattern, while the rainfall over land exhibits significant departures from

this cycle. During phases 1–4 when OLR is suppressed and rainfall is high over the GoG, there are regions of suppressed rainfall in equatorial Africa and West Africa. In contrast, during phases 5–8 when OLR is enhanced and rainfall is suppressed over the GoG, rainfall can be more active in some regions over the land. These spatial differences are illustrated more specifically by the anomaly pattern of phase 8: here, rainfall remains suppressed over the GoG, consistent with high OLR, and is likewise suppressed over most of East Africa (boxes D, F, H) and west south-central Africa (box G), but rainfall is enhanced over West Africa (box B) and west equatorial Africa (box E) (with approximately the reverse in phase 4).

The continental-scale patterns in rainfall anomalies for the P25 and CP4 simulations (Fig. 5) broadly match the continental-scale patterns in TRMM rainfall. The P25 rainfall anomalies are smaller than the TRMM anomalies, consistent with the weaker OLR anomalies (Fig. 2d) and the smaller variance in CCKW-filtered OLR across the equatorial latitudes (Figs. 2e,f) in the G25 simulation compared to observations. In CP4, there is more grid-scale spatial variability than in TRMM and

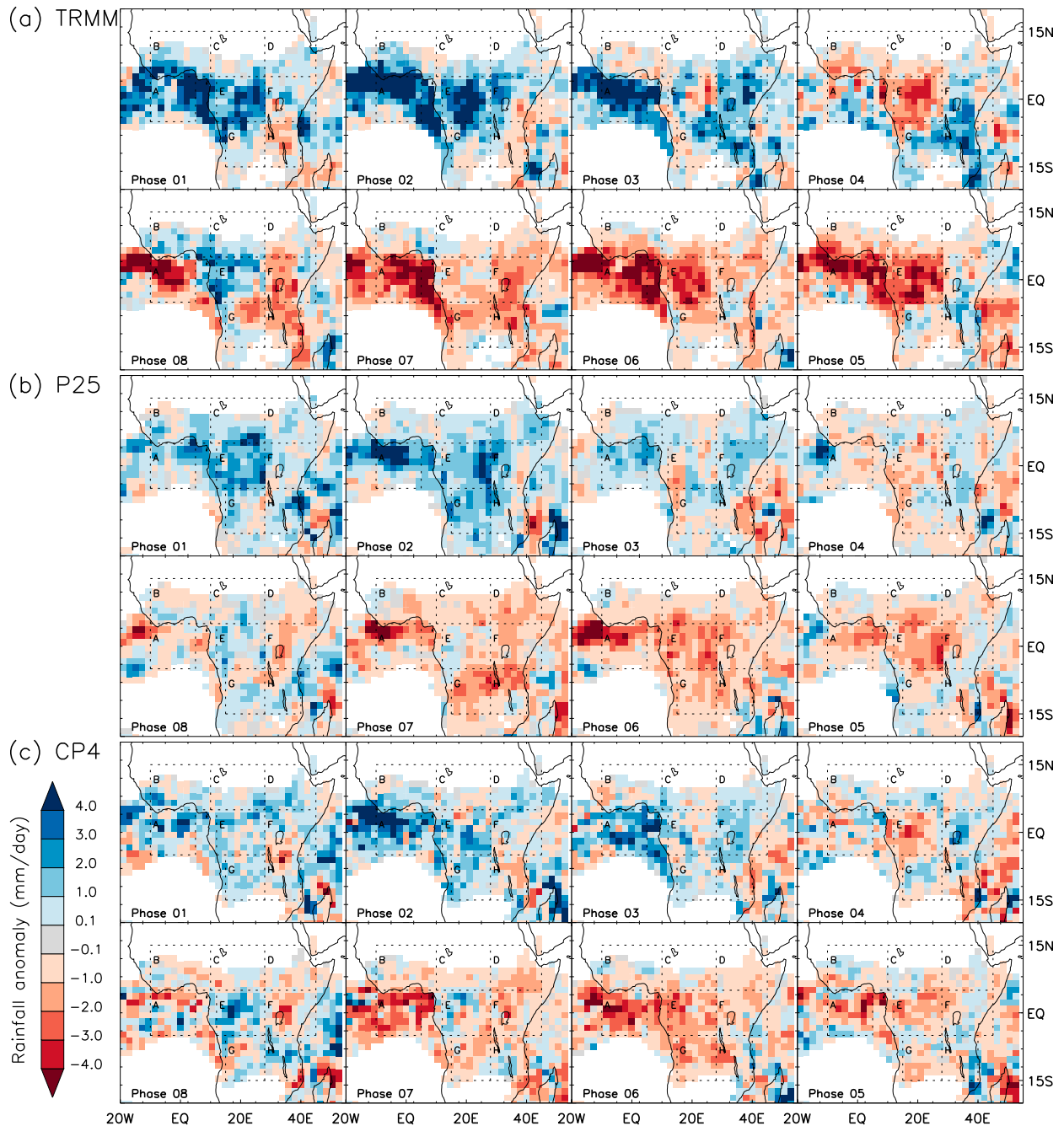


FIG. 5. The difference between the mean rainfall in each phase of the Kelvin wave and the April monthly mean rainfall for (a) TRMM observations, (b) the P25 simulation, and (c) the CP4 simulation at 150-km resolution. The regions labeled A–H are the Gulf of Guinea (A), West Africa (B), north-central Africa (C), east north-central Africa (D), west equatorial Africa (E), east equatorial Africa (F), west south-central Africa (G), and east south-central Africa (H).

P25 such that the clusters of positive and negative anomalies are less homogeneous, even on the 150-km grid used in Fig. 5.

Regional-scale differences in the spatial distribution of rainfall anomalies between TRMM and the P25 and

CP4 simulations may be due, in part, to differences in the locations of the tropical rain belt (Figs. 3c,e). There are also distinct regional-scale differences in TRMM rainfall anomalies that we describe, below, for those regions with the strongest rainfall response to CCKWs.

- 1) WEST AFRICA–GOG DIPOLE (FIG. 5, BOX B, 10°W–10°E, 5°–15°N AND BOX A, 10°W–5°E, 5°S–5°N)

Over West Africa, the TRMM rainfall anomalies transition from suppressed to enhanced in phases 7 and 8 of the CCKW cycle, one or two phases before the same transition over the GoG and the phase of minimum OLR. Similarly, in phases 2 and 3, the TRMM rainfall anomalies change from enhanced to suppressed before suppression of rainfall occurs over the GoG. This results in a dipole in the rainfall anomaly with a shift of rainfall onshore in phase 8 and a shift offshore in phase 4. This dipole is not well represented by the P25 and CP4 simulations. Both simulations have changes in rainfall anomalies that are largely in phase with the changes over the GoG. The implications are that the passage of a CCKW leads to a shift of the rain belt northward as the CCKW begins to enhance rainfall and southward over the ocean as the CCKW begins to suppress rain. This spatial pattern of response, which we surmise could be important in monsoon onset, is not well captured in the models.

- 2) WEST EQUATORIAL AND WEST SOUTH-CENTRAL AFRICA (FIG. 5, BOX E, 12°–28°E, 5°S–5°N AND BOX G, 15°–28°E, 15°–5°S)

The TRMM rainfall anomalies are large in west equatorial Africa relative to other continental regions. The variance in total rainfall anomaly (Fig. 3b) is also large and the equatorial location ensures strong interactions between the mesoscale storms and the equatorially trapped CCKWs. Similar to West Africa, the transition in rainfall anomalies between enhanced and suppressed rainfall occurs one phase before the transition in OLR in the CCKW cycle, and one phase before the rainfall transition over the GoG. There is also a dipole in rainfall anomaly between west equatorial Africa and west south-central Africa that involves a northward shift in rainfall in phase 8, and a southward shift in phases 3 and 4. In contrast to West Africa, the P25 and CP4 simulations successfully capture the CCKW cycle in rainfall anomaly over west equatorial Africa and therefore capture the modulation of the land–sea dipole between boxes A and E.

In addition to the overall pattern in boxes E and G, there is a distinct change in the rainfall response along the coastal strip of box G (Angola) where the rainfall transitions occur one phase earlier than farther inland. This spatial pattern of response is captured in the models over north Angola but not farther south.

- 3) EAST EQUATORIAL AND EAST SOUTH-CENTRAL AFRICA (FIG. 5, BOX F, 28°–45°E, 5°S–5°N AND BOX H, 28°–40°E, 15°–5°S)

Over east equatorial Africa, the transition in TRMM rainfall anomalies between enhanced and suppressed rainfall is mostly synchronized with the CCKW cycle in OLR and also with rainfall anomalies over the GoG. There is a sharp contrast, therefore, between rainfall anomalies in east and west equatorial Africa ($\sim 28^\circ\text{E}$) that is particularly clear in phases 8, 3, and 4. The area located at $\sim 3.5^\circ\text{N}$ and $\sim 41^\circ\text{E}$, which is southeast of the Ethiopian highlands, is an exception. Here, the cycle in rainfall anomalies mirrors the CCKW cycle over west equatorial Africa. The P25 and CP4 simulations represent well the CCKW cycle in TRMM rainfall over east equatorial Africa.

In the east south-central region (box H), the TRMM rainfall anomalies change between suppressed and enhanced rainfall one phase after the change between enhanced and suppressed OLR in the CCKW cycle. Rainfall does not change from suppressed to enhanced until phase 3 and rainfall remains enhanced until phase 5. There are some traces of a dipole in rainfall anomaly between east south-central and east equatorial Africa that involves a northward shift in rainfall in phases 1 and 2, and a southward shift in phase 5, although this dipole is not as robust as the dipole between the GoG (box A) and West Africa (box B). The CCKW cycle of rainfall anomalies is not well represented in the P25 and CP4 simulations. The simulations do not produce distinct changes between suppressed and enhanced rainfall and in most phases there are gridcell anomalies of both positive and negative signs.

d. The relationship between rainfall anomaly and CCKW activity

Figures 6a–c show the mean anomaly averaged over latitudes 15°S–15°N based on the “local” phase at each longitude and give a meridional average view of the spatial relationships in rainfall anomaly shown in Fig. 5. To show the pattern of rainfall anomalies as they typically occur across Africa, Figs. 6d–f show the mean anomaly, as in Figs. 6a–c, except that they are based on the occurrence of a CCKW phase at a chosen reference meridian through continental Africa, at 25°E. The rainfall anomaly at each longitude is calculated based on the local phase that coincides most frequently with the phase prevalent at the reference meridian. Figures 6g and 6h show this local modal phase for observations and the G25 simulation. To illustrate the method, the top row of Fig. 6g shows the CCKW phases that occur most frequently at each longitude when phase

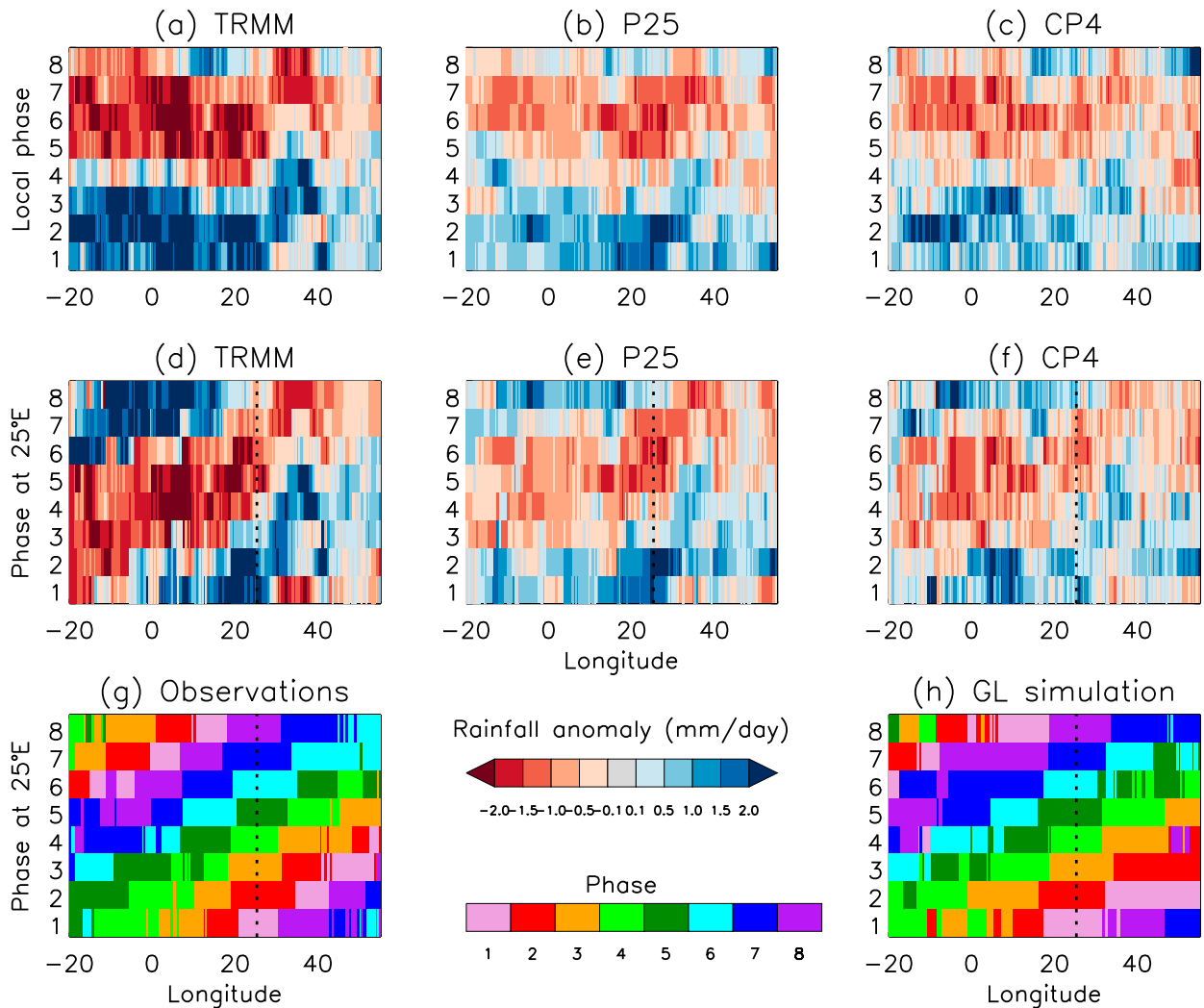


FIG. 6. The mean rainfall anomalies for each local CCKW phase averaged over latitudes 15°S – 15°N for (a) TRMM, (b) P25, and (c) CP4. (d) The mean rainfall anomalies at each longitude (averaged over latitudes 15°S – 15°N) for each phase of the Kelvin wave at 25°E for TRMM. (e) As in (d), but for P25. (f) As in (d), but for CP4. (g) The CCKW phases for the NOAA OLR observations that occur most frequently at each longitude given the phase current at 25°E (marked by the dashed line) where the rows represent the phase current at 25°E . (h) As in (g), but for the G25 simulation.

8 is prevalent at 25°E and these phases were used to calculate the rainfall anomalies shown in the top row of Fig. 6d.

Figures 6d–f highlight the eastward propagation of the rainfall anomalies and illustrate the spatial (east–west) extent of rainfall anomalies. There are sharp contrasts in rainfall anomalies both between neighboring regions (e.g., between 25° and 30°E in phase 1) and from one phase to another on a meridian (e.g., between phases 1 and 2 at 30°E). Although the CCKW wavelengths exceed the width of the domain, with seven of the eight phases typically spanning the equator from 20°W to 55°E (Fig. 6g), only half a CCKW wavelength is needed to produce these sharp contrasts in rainfall, particularly for

TRMM observations with their relatively large amplitude in rainfall anomaly.

The G25 simulation (Fig. 6h) has a similar pattern to the observations although the CCKW wavelengths are longer. When the phase in the G25 simulation is the same as the phase in NOAA observations at 25°E , the phases at 20°W and 55°E are frequently one phase out in G25. This will account for some of the differences in rainfall anomalies between TRMM and the P25 and CP4 simulations.

There is a dramatic spatial spread in the wave phase of peak TRMM rainfall anomaly (Fig. 7a). The greatest enhancement in TRMM rainfall (Fig. 7a) generally occurs in phases 1 and 2 over West Africa, west equatorial

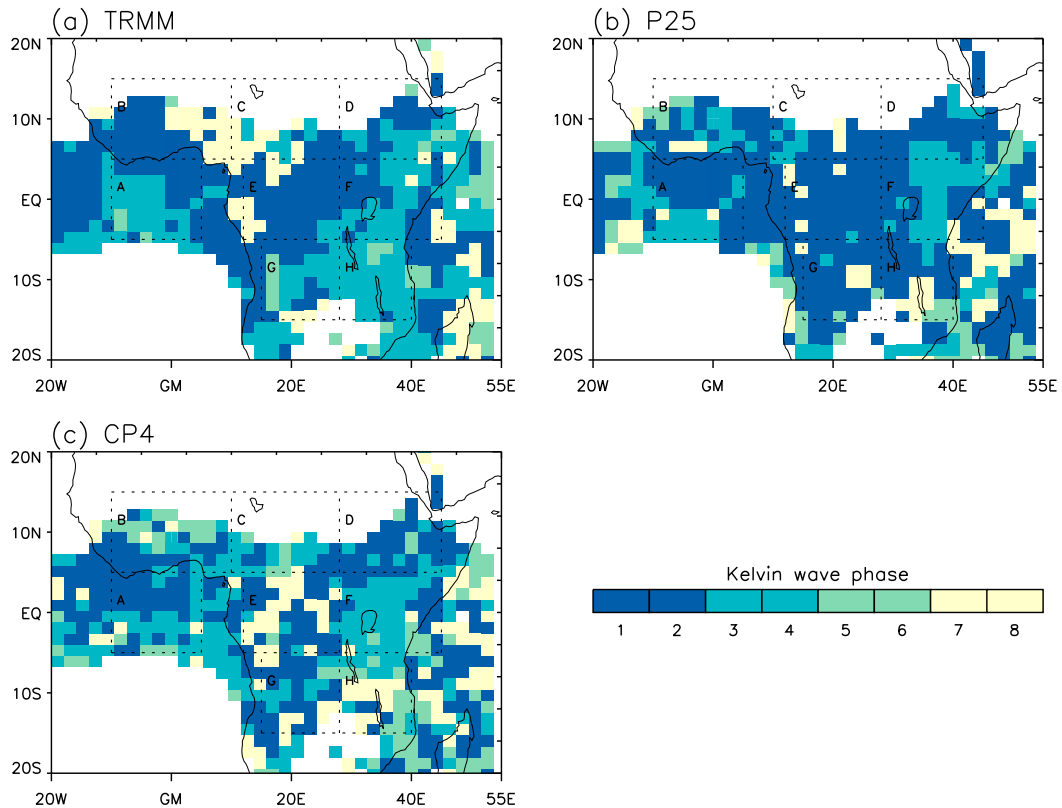


FIG. 7. The Kelvin wave phases in which the maximum enhancement to rainfall occurred for (a) TRMM observations, (b) the P25 simulation, and (c) the CP4 simulation at 150-km resolution.

Africa, and coastal regions over the GoG. In contrast, rainfall anomalies peak in phases 3 and 4 over east equatorial Africa, east south-central Africa and over the GoG (remote from the coast). Relative to the wave, the very latest peaks, around phase 4 and even phase 5, are generally in the south and east, with earlier peaks, around phases 7 and 8, in eastern West Africa on the boundaries of zones B and C (Nigeria and Cameroon) and along the coast of west equatorial Africa (e.g., Gabon).

P25 has a broadly similar pattern over equatorial Africa capturing the differences between east and west (Fig. 7b). CP4 performs better than P25 in that it captures the peaks in phases 7 and 8 near the coast of west equatorial Africa (western edge of box E) although it performs less well farther east (e.g., over the Congo basin) (Fig. 7c). The similarity to TRMM is markedly poorer for both simulations, however, along a northwest–southeast axis from West Africa to Mozambique. The simulations do not capture well the later peaks in the south and east or the earlier peaks in the west. These differences suggest that the models do not capture well the meridional variation in the propagation of CCKW dynamics.

e. Impact of CCKWs on rainfall variability

In this section, the change in rainfall at each phase of the CCKWs is split into two components: the change in the percentage of days that have rainfall less than a threshold of 0.1 mm day^{-1} (dry-day frequency) and the change in the rainfall intensity on rainy days (wet-day intensity).

CCKWs affect TRMM rainfall through changes in both the frequency of dry days (Fig. 8) and the intensity of rain on rainy days (Fig. 9). Both measures contribute to large-scale reductions in rainfall during CCKW phases 5–7 and enhanced rainfall during phases 1–3 and indicate that CCKW activity modulates both the initiation and intensification of rainstorms over tropical Africa. Further, both measures contribute to opposing changes over west equatorial and east equatorial Africa during phases 4 and 8.

The frequency of occurrence of dry days is significantly different between phase 2 and phase 7 in a paired Student's t test at the 1% significance level for TRMM, P25, and CP4. However, the P25 simulation does not capture well the pattern of dry-day frequency in TRMM (Fig. 8). Changes over equatorial Africa are small in

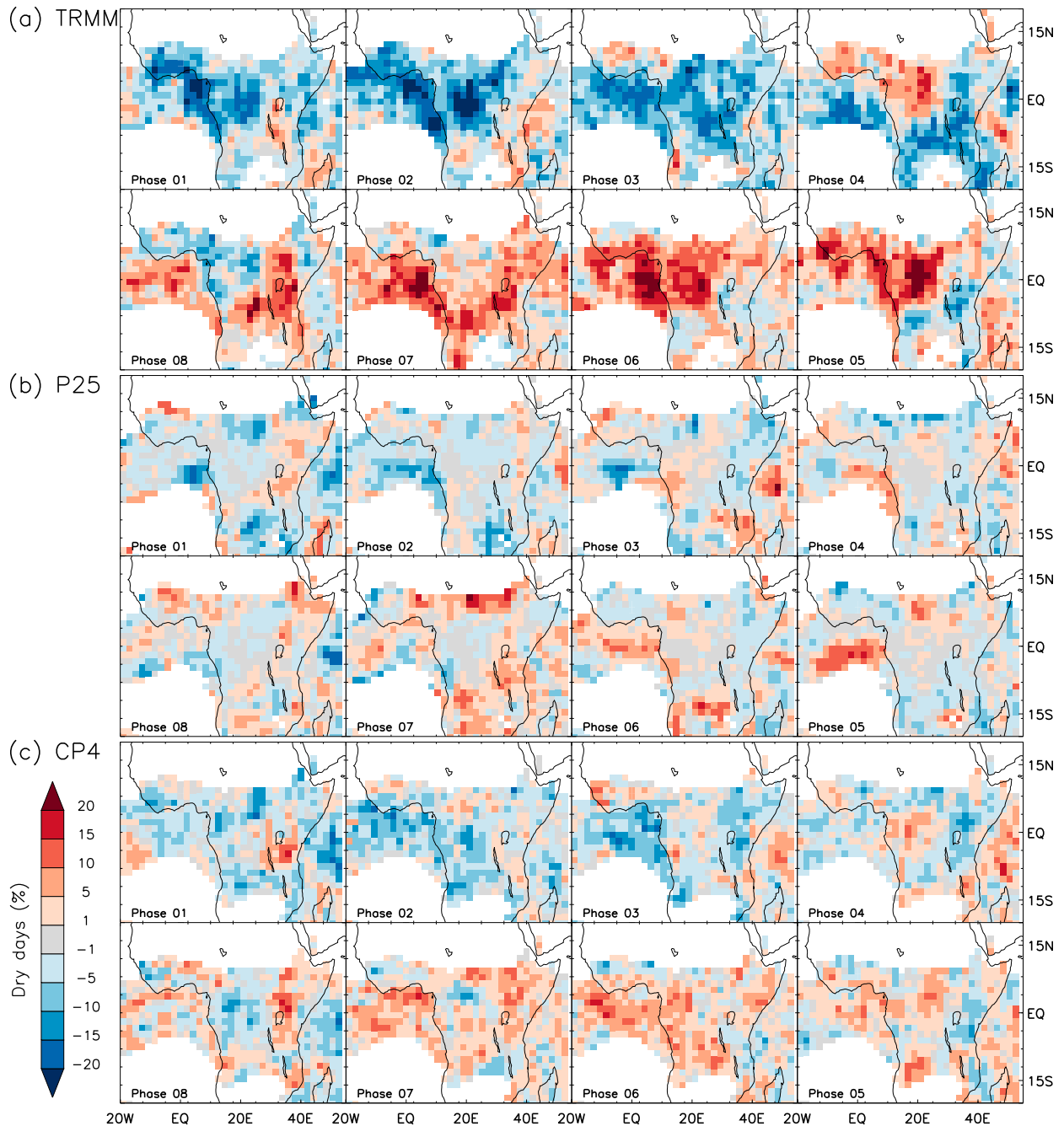


FIG. 8. The difference between the frequency of occurrence of dry days (expressed as a percentage) in each phase of the Kelvin wave relative to the April monthly mean for (a) TRMM observations, (b) the P25 simulation, and (c) the CP4 simulation at 150-km resolution.

magnitude and do not mimic the response to CCKW activity in TRMM. The few relatively large changes in dry days are located near the margins of the rain belt or over the oceans. In contrast, CP4 captures the large-scale spatial patterns and relationships with CCKW activity in dry-day frequency (Fig. 8) although the magnitude of the changes is less than in TRMM.

The anomalies in wet-day intensity for the P25 simulation (Fig. 9) capture the main regions where large changes occur in TRMM and also their relationships with CCKW activity. The magnitude of these changes, however, is very weak. Similarly, the CP4 simulation captures the large-scale patterns and phase relationships in wet-day intensity. The

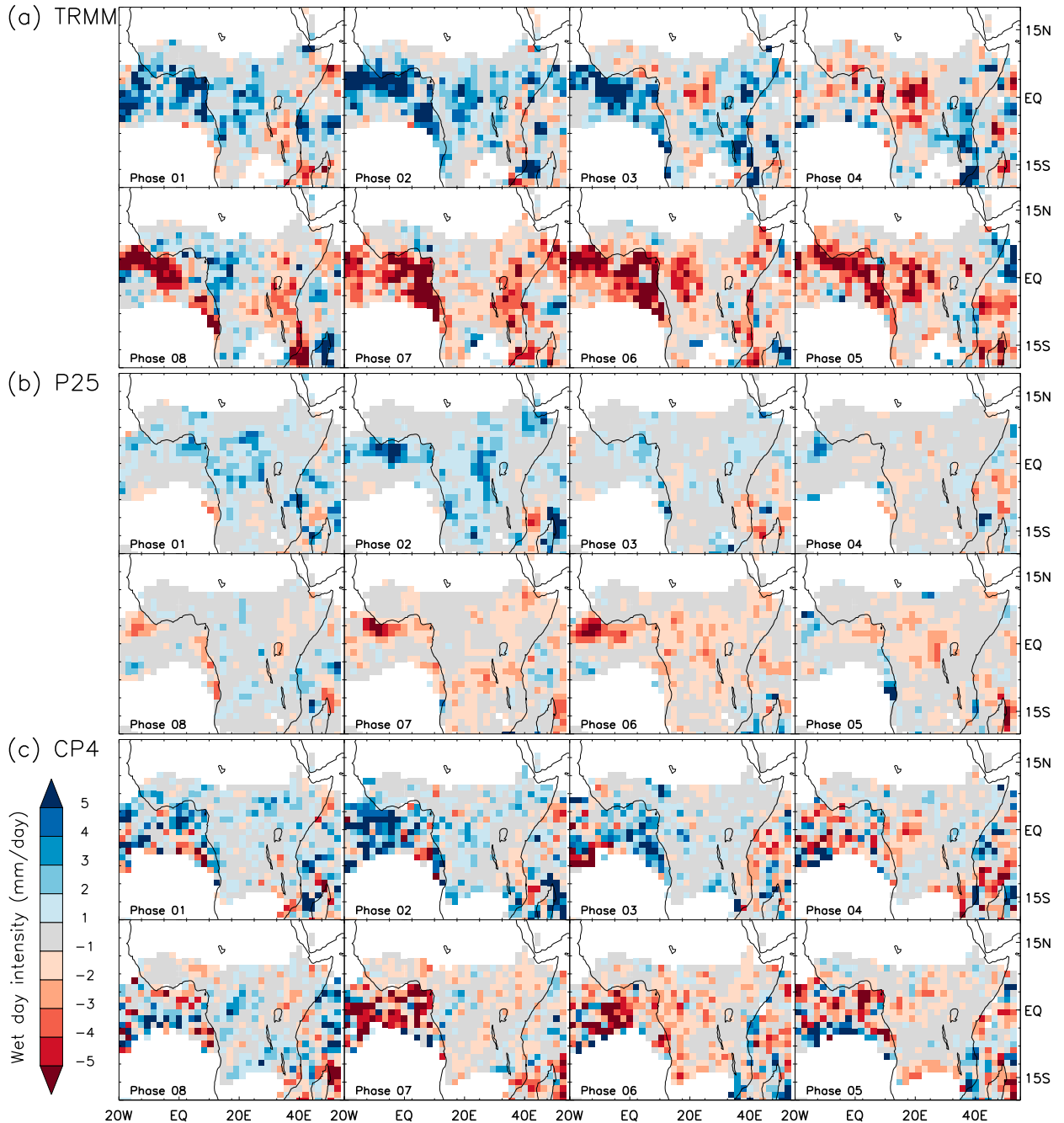


FIG. 9. The difference between wet-day rain intensity in each phase of the Kelvin wave relative to the April monthly mean for (a) TRMM observations, (b) the P25 simulation, and (c) the CP4 simulation at 150-km resolution.

magnitude of the changes over land in CP4 is weaker than TRMM and there are numerous grid-scale variations from TRMM.

f. Impact of CCKWs on extreme rainfall

In this section, we show the impact of CCKWs on a measure of moderate extreme rainfall: the total daily

rainfall that exceeded the 95th percentile of wet-day rainfall (R95p), a measure defined in Alexander et al. (2006) and described as an index of “very wet days.” Figure 10 shows the percentage of R95p rainfall that occurs in each phase of the CCKW for TRMM, P25, and CP4. The distribution of R95p rainfall between the eight phases shows that CCKW activity enhances and

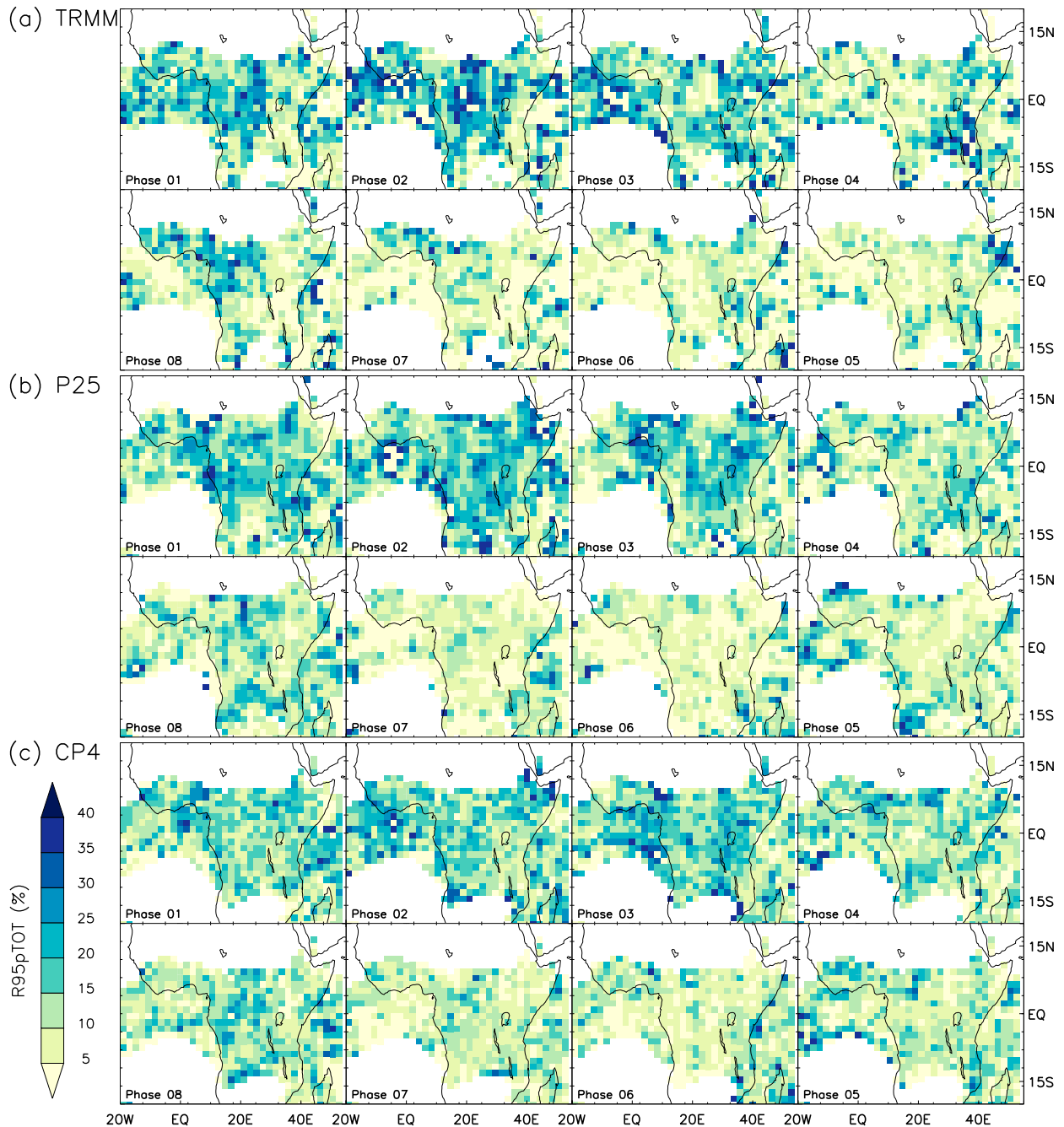


FIG. 10. The percentage split between Kelvin wave phases of the total daily rainfall that exceeded the 95th percentile of wet-day rainfall (R95pTOT) for (a) TRMM observations, (b) the P25 simulation, and (c) the CP4 simulation. Rainfall is for the month of April and the grid resolution is 150 km. The percentages in each grid cell sum to 100% over the eight phases.

suppresses R95p rainfall. The percentages of R95p rainfall in phase 2 and phase 7 are significantly different in a paired Student's t test at the 1% significance level for TRMM, P25, and CP4. As shown for mean rainfall (Fig. 5), both P25 and CP4 underestimate the amplitude of anomalies in R95p compared to TRMM.

g. Dynamical processes

We present anomalies in each phase of the CCKW cycle for vertical motion and zonal winds (Fig. 11) for three selected equatorial regions: west equatorial Africa (WEA), east equatorial Africa (EEA), and the GoG

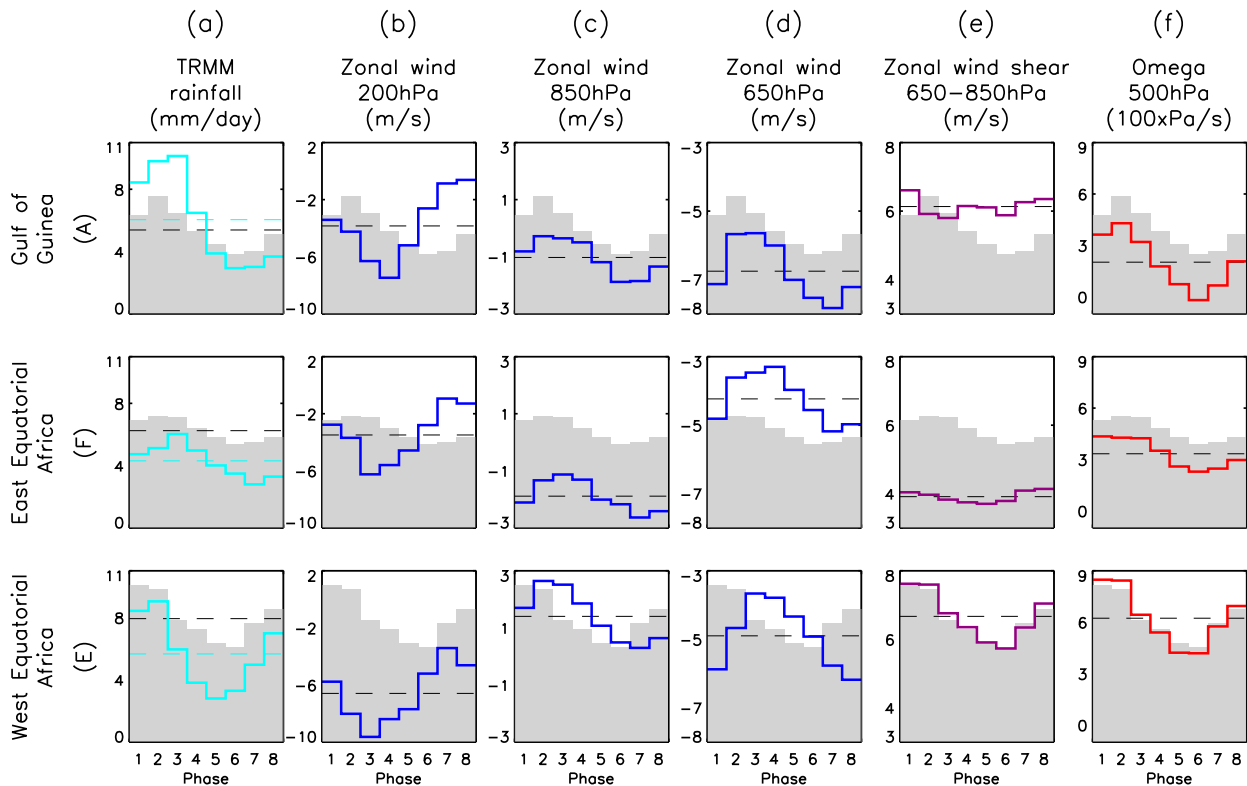


FIG. 11. The mean Kelvin wave cycle for rainfall and model diagnostics. The rows show values for three equatorial regions. The P25 rainfall anomalies are represented by the gray shaded bars. (a) The Kelvin wave cycle for TRMM rainfall (cyan) with the TRMM mean rainfall represented by the cyan dashed line and the P25 mean rainfall by the black dashed line. (b)–(f) Mean values by phase for modeled diagnostics overlaid as colored solid lines and their April monthly means represented by the black dashed lines.

(regions E, F, and A of Fig. 5, respectively). We present results from the P25 simulation; results from the CP4 simulation are qualitatively similar and the same general conclusions would be reached from study of either model. The phasing of P25 rainfall anomalies and TRMM anomalies is closely matched in the three regions (Fig. 11, column a). The amplitude of the rainfall anomalies, however, is greater in TRMM as shown in Fig. 5.

The CCKWs diagnosed in OLR are closely coupled with the zonal wind anomalies in all regions, which indicates that OLR is a robust indicator of the underlying dynamical CCKWs. At 200 hPa (Fig. 11, column b), peak westerly zonal wind anomalies occur in phases 7 and 8 and upper-level divergence, with its transition from westerly to easterly anomalies, occurs approximately in phase 2. Peak easterly anomalies occur in phases 3 and 4 and upper-level convergence in phase 6. At 850 hPa (Fig. 11, column c), the zonal wind anomalies are the reverse of those at 200 hPa with a lag of ~ 1 phase at 200 hPa compared to 850 hPa (e.g., the change from westerly to easterly anomalies at 850 hPa occurs in phase 5, whereas the reverse change at

200 hPa generally occurs in phase 6). The zonal circulation of the CCKWs is tilted in the troposphere (up to ~ 200 hPa) from the east (low levels) toward the west (upper levels) and may be due to interactions between diabatic heating and vertical advection (Kiladis et al. 2009). Maps of the wind anomalies at 850 hPa (Fig. 12a) show that anomalies in the zonal wind component are stronger in the vicinity of the equator and that anomalies in the meridional component are stronger away from the equator.

Rainfall over WEA responds differently to CCKW forcing than rainfall over EEA and the GoG (Fig. 5). In particular, the transition to enhanced rainfall over WEA occurs earlier than over the other two regions, in phase 8, when OLR remains enhanced, compared to phase 1 over the GoG and EEA. Strong zonal wind anomalies are prevalent during phase 8 over WEA at 850 hPa (easterly) and 200 hPa (westerly). Midtropospheric winds at 650 hPa (Fig. 12b), described as the African easterly jet (AEJ) when at a seasonal maximum, contribute to the organization of storms and the enhancement or suppression of convection through their seasonal migration, propagation of African easterly

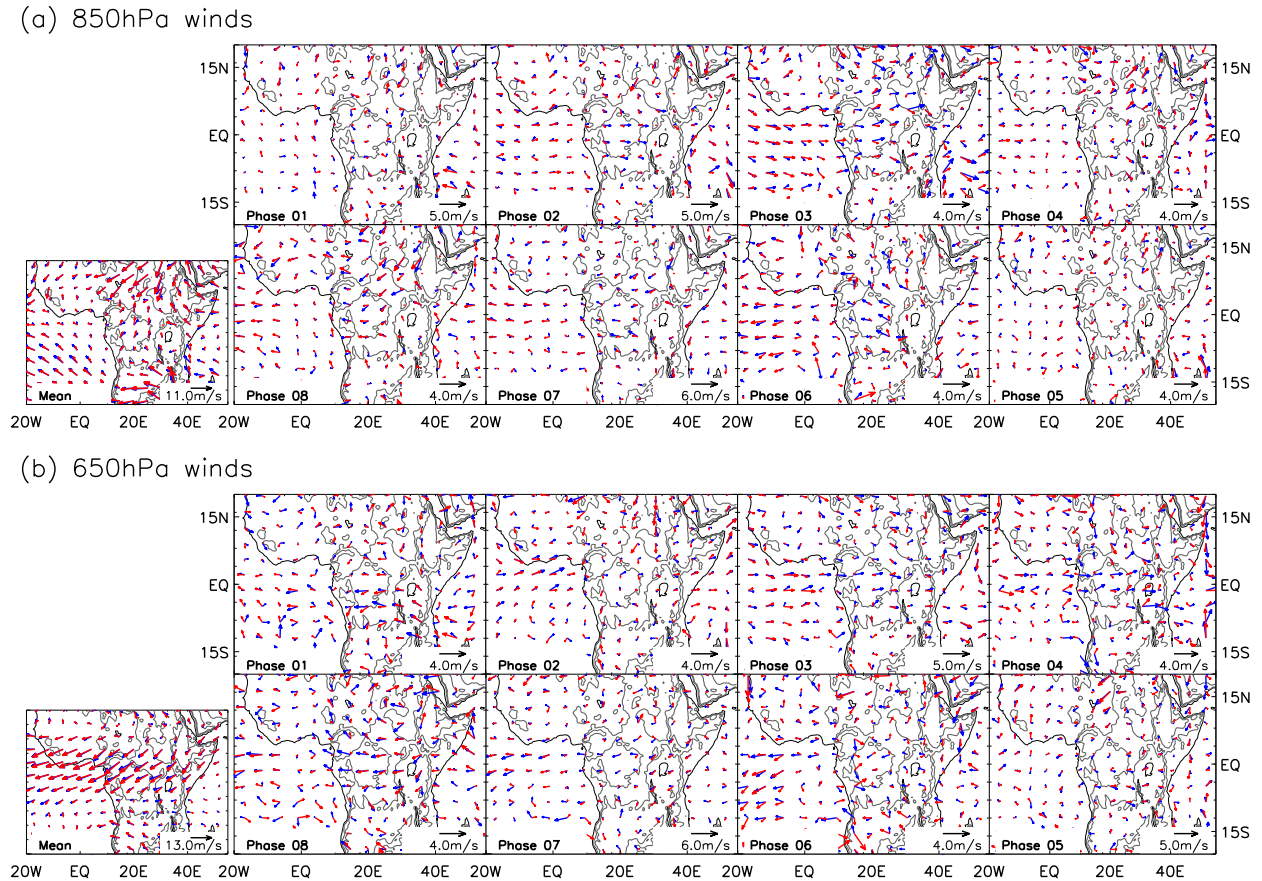


FIG. 12. (a) The mean anomaly in horizontal winds for each Kelvin wave phase relative to the April monthly mean on the 850-hPa pressure level. (b) As in (a), but for the 650-hPa pressure level. The April mean winds averaged over all phases are shown in the far left-hand column. The horizontal winds for P25 are represented by blue arrows and CP4 by red arrows.

waves, and modulation of midlevel humidity and vertical wind shear (Tompkins et al. 2005). The majority of enhanced rainfall over WEA occurs when an easterly anomaly is prevalent at 650 hPa (Fig. 11, column d) and, during the transition to enhanced rainfall in phase 8, the prevailing midlevel easterly winds over WEA (Fig. 12b) are enhanced by the anomalous easterlies. Further, rainfall anomalies are closely synchronized with the CCKW cycle in vertical wind shear (650- and 850-hPa zonal winds) over WEA (Fig. 11, column e). The easterly wind anomalies are closely associated with enhanced vertical wind shear and the enhanced rainfall over WEA is sustained while the enhanced shear persists. Rainfall over WEA is dominated by MCSs (Jackson et al. 2009) that may be favored by shear and the transition to enhanced rainfall could be associated with the transition to enhanced shear. Vertical velocity (500 hPa) and rainfall are closely coupled in all regions (Fig. 11, column f). As for rainfall, the transition to intensified upward

motion over WEA occurs earlier in the CCKW cycle than over the other regions.

Over the GoG and EEA, the transition to enhanced rainfall is coincident with low-level convergence and upper-level divergence in wind anomalies. The coupling of rainfall and midlevel wind is weaker than over WEA (Fig. 11, column d). Rainfall lags shear and climatological wind shear is weaker over EEA than farther west (Fig. 11, column e). The surface is more moisture-limited in EEA, there are significant mountains and lakes that dominate convective triggering, and a higher proportion of rainfall comes from shorter-lived (Laing et al. 2011) and less-organized (Nesbitt et al. 2006) systems. It is likely, therefore, that such systems are not enhanced by shear over EEA.

h. Performance of the parameterized versus convection-permitting simulations

Figure 13 shows a Taylor diagram for the P25 and CP4 rainfall anomalies compared to TRMM observations.

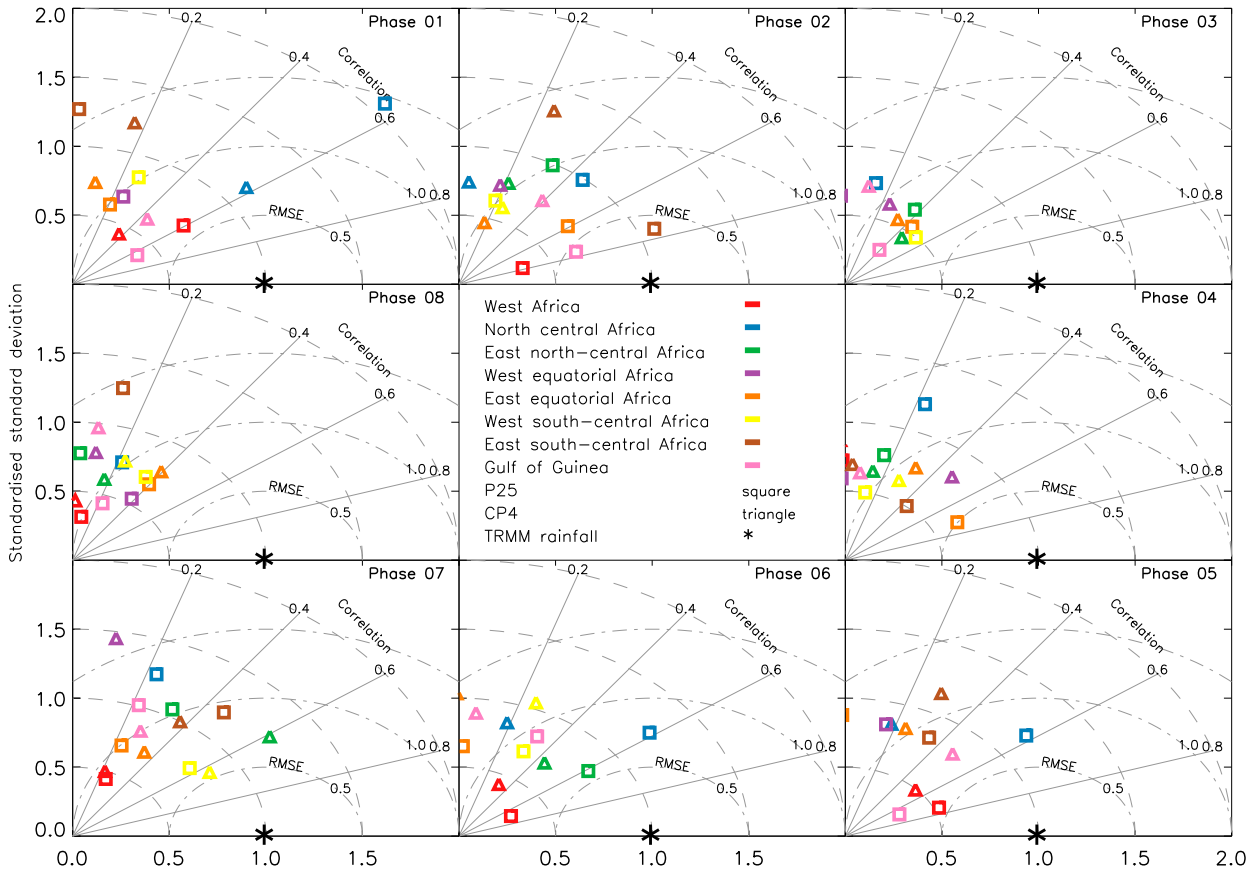


FIG. 13. Taylor diagrams at 150-km resolution for P25 and CP4 rainfall anomalies by Kelvin wave phase compared to TRMM rainfall anomalies. The x and y axes show standard deviations of rainfall anomalies over the grid cells within each region. The standard deviations have been standardized so that the TRMM anomaly standard deviation is 1.0 in each phase and each region. Spatial correlation is shown by the polar coordinate scale centered on $(0, 0)$ and represented by the dashed gray curves. Root-mean-squared error (RMSE) is shown by the polar coordinate scale centered on $(1, 0)$ and represented by the dot-dashed gray curves.

Spatial correlations are shown on the polar coordinate scale centered on the $(0, 0)$ point; only positive correlations are shown. In each CCKW phase, the majority of spatial correlations are positive and approaching 50% of the correlations exceed 0.2. The strongest correlations are from P25 in most phases. Standard deviations are shown on the x axis. Both P25 and CP4 underestimate the standard deviation with several points less than 50% of the standardized TRMM standard deviation. There is little to choose between the two simulations. The root-mean-squared errors (RMSEs) are shown on the polar coordinate scale centered on the $(1, 0)$ point. Except for phases 4 and 7, the P25 simulation has more small RMSEs than CP4 (i.e., less than 1.0). Overall, therefore, the P25 simulation outperforms the CP4 simulation. No region or phase stands out as being consistently closer to TRMM data.

Although the TRMM data point is marked with a correlation and standard deviation of one, it would be

unrealistic to expect any simulation to consistently achieve that level of accuracy due to variability within the TRMM data and also due to systematic errors in TRMM. To illustrate the effect of variability, $\sim 10\%$ of resamples of TRMM data were found to have a correlation less than 0.9 using bootstrap resampling. In the calculation of spatial correlations, the RCM simulations are penalized for near-neighbor differences in gridpoint rainfall anomalies. This was mitigated, to some extent, by coarse graining the TRMM, P25, and CP4 data to a common 150-km grid. Indeed, the spatial correlations are stronger on the 150-km grid resolution than 25 km (not shown).

4. Discussion and conclusions

The amplitude of CCKWs in observed OLR anomalies is greatest in April and accounts for $\sim 15\%$ of the variance in TRMM daily rainfall. CCKWs strongly

influence anomalies in mean rainfall, the frequency of occurrence of dry days, wet-day rain intensity, and the occurrence of extreme rainfall. CCKWs, therefore, likely play an important role in the March–May rainy seasons in west and east equatorial Africa through intraseasonal breaks and extreme rain events and, may influence the timing and intensity of the subsequent coastal phase of the WAM in May and June and the onset of the WAM over the Sahel region in July. It is necessary for the realistic simulation of rainfall variability over tropical Africa, therefore, that climate models realistically simulate CCKWs. Indeed, the realistic simulation of tropical wave modes in general is important because the passage of CCKWs over tropical Africa frequently occurs in combination with other tropical wave modes (e.g., Janicot et al. 2010; Lafore et al. 2017; Schlueter et al. 2019a).

Our results identify marked regional differences in the response of rainfall to CCKW forcing even when the dynamical responses are consistent. Over West Africa there is a dipole corresponding to onshore/offshore shifts in rainfall. Rainfall is enhanced relatively early in the CCKW cycle over WEA in contrast to rainfall enhancement over EEA. The differences in regional rainfall responses to CCKWs present a challenge to climate models. The dipole over West Africa was not well represented by either simulation and may indicate the absence of a teleconnection identified in reanalyses that links convection over West Africa with convection over the Congo basin (Cook and Vizy 2016). Neither simulation captured well the timing of peak rainfall anomalies away from the equatorial regions that tended to be early in the north and west and late in the south and east. Replacing parameterized convection with explicit convection did not resolve these issues. Improvements may come from resolving finer-scale regional variations, for example, as identified by Hogan et al. (2015) for the MJO cycle over coastal and highland regions of East Africa, and ultimately likely yield improved rainfall prediction at ~2-day lead time.

Explaining the dynamical causes of the differing regional responses in rainfall will require a closer examination of the dynamics of convective rainfall in response to these drivers, perhaps through idealized high-resolution modeling studies, or detailed climatologies of storm types. While beyond the scope of this study, we note the strong association of enhanced wind shear and strengthened midlevel easterlies with the enhanced rainfall and CCKW activity that prevailed over WEA. Differences in the dynamics of MCSs between WEA and EEA, including the role of vertical shear and mid-level dry advection (not considered in this study), and their relationships with CCKW activity are key areas for

further research. We also note that the influence of cirrus cloud on OLR needs further investigation due to the tendency for cirrus cloud to persist after convection (Roundy and Frank 2004).

The P25 and CP4 simulations reproduced the large-scale perturbations of TRMM rainfall by CCKWs. Both simulations, however, underestimated the magnitude of rainfall anomalies and also the proportion of rainfall variance associated with CCKWs. The P25 simulation performed better than CP4 in terms of spatial correlations and RMSE errors. While CP4 simulated anomalies with greater amplitude than P25, greater spatial variability between near-neighbor grid cells weakened its spatial correlation with TRMM. The CP4 simulation performed better than P25 in reproducing the CCKW cycle in the number of dry days. Similarly, Birch et al. (2016) found no improvement in the simulation of local-scale responses to remote forcing in convection-permitting simulations over the Maritime Continent. This may not apply in all climate models, however. CCKW dynamics are very sensitive to adjustment-based closure in convective parameterizations (Straub et al. 2010). Parameterized convection may not perform so well for other types of tropical waves: For example, McCrary et al. (2014) found that a climate model with superparameterized convection captured strong African easterly wave activity absent from simulations using parameterized convection.

It is expected that rainfall over tropical Africa will become more intense, and in many places less frequent, due to climate change during the twenty-first century (Niang et al. 2014; Kendon et al. 2019). The systematic organization of rainfall into spells of more and less intense rain by CCKWs, as described in this study, suggests that CCKWs will likely be more influential in the future climate of tropical Africa.

Acknowledgments. The authors were supported by Natural Environment Research Council/Department for International Development (NERC/DFID, NE/MO17176/1, NE/M017214/1, and NE/M02038X/1) via the Future Climate for Africa (FCFA) funded projects: Improving Model Processes for African Climate (IMPALA) and Integrating Hydro-Climate Science into Policy Decisions for Climate-Resilient Infrastructure and Livelihoods in East Africa (HyCRISTAL). Jackson and Marsham were also supported by the DACCIWA project. DACCIWA funding from the European Union Seventh Framework Programme (FP7/2007-2013) under Grant Agreement 603502 (EU project DACCIWA: Dynamics-aerosol-chemistry-cloud interactions in West Africa). Parker was supported by a Royal Society Wolfson Research Merit

Award. The contribution of Richard Keane was performed within the Centre of Excellence for Modelling the Atmosphere and Climate (CEMAC), University of Leeds. We thank Malcolm Roberts (Met Office) for running the N512-resolution AMIP global simulation; Prince Xavier for his Python version of the NCL spectral analysis code wkSpaceTime used to produce Fig. 1; Charly Schreck for contributing the NCL code kf_filter, which was used to produce the CCKW-filtered OLR anomalies; and Peter Willets for help in processing TRMM data. We also acknowledge the NASA Goddard Space Flight Center's Precipitation Measurement Missions and PPS for provision of the TRMM 3B42, version 7, dataset; ECMWF for the ERA-Interim dataset; and the Physical Sciences Division of NOAA/OAR/ESRL, Boulder, Colorado, for provision of the NOAA interpolated OLR dataset. Output from the model simulations will be made publicly available from July 2019. Finally, we thank A. Aiyyer and two anonymous reviewers for their comments, which greatly improved the clarity of the paper.

REFERENCES

- Alexander, L. V., and Coauthors, 2006: Global observed changes in daily climate extremes of temperature and precipitation. *J. Geophys. Res.*, **111**, D05109, <https://doi.org/10.1029/2005JD006290>.
- Berthou, S., D. P. Rowell, E. J. Kendon, M. J. Roberts, R. A. Stratton, J. A. Crook, and C. Wilcox, 2019: Improved climatological precipitation characteristics over West Africa at convection-permitting scales. *Climate Dyn.*, **53**, 1991–2011, <https://doi.org/10.1007/S00382-019-04759-4>.
- Birch, C. E., D. J. Parker, J. H. Marsham, D. Copley, and L. Garcia-Carreras, 2014: A seamless assessment of the role of convection in the water cycle of the West African monsoon. *J. Geophys. Res. Atmos.*, **119**, 2890–2912, <https://doi.org/10.1002/2013JD020887>.
- , S. Webster, S. C. Peatman, D. J. Parker, A. J. Matthews, Y. Li, and M. E. E. Hassim, 2016: Scale interactions between the MJO and the western Maritime Continent. *J. Climate*, **29**, 2471–2492, <https://doi.org/10.1175/JCLI-D-15-0557.1>.
- Blanco, J. E., D. S. Nolan, and B. E. Mapes, 2016: Convectively coupled Kelvin waves in aquachannel simulations: 2. Life cycle and dynamical-convective coupling. *J. Geophys. Res.*, **121**, 11 319–11 347, <https://doi.org/10.1002/2016JD025022>.
- Cook, K. H., and E. K. Vizy, 2016: The Congo basin Walker circulation: Dynamics and connections to precipitation. *Climate Dyn.*, **47**, 697–717, <https://doi.org/10.1007/s00382-015-2864-y>.
- Davies, T., 2014: Lateral boundary conditions for limited area models. *Quart. J. Roy. Meteor. Soc.*, **140**, 185–196, <https://doi.org/10.1002/qj.2127>.
- Finney, D. L., and Coauthors, 2019: Implications of improved representation of convection for the East Africa water budget using a convection-permitting model. *J. Climate*, **32**, 2109–2129, <https://doi.org/10.1175/JCLI-D-18-0387.1>.
- Frierson, D. M. W., D. Kim, I.-S. Kang, M.-I. Lee, and J. Lin, 2011: Structure of AGCM-simulated convectively coupled Kelvin waves and sensitivity to convective parameterization. *J. Atmos. Sci.*, **68**, 26–45, <https://doi.org/10.1175/2010JAS3356.1>.
- Gregory, D., and P. R. Rowntree, 1990: A mass flux convection scheme with representation of cloud ensemble characteristics and stability-dependent closure. *Mon. Wea. Rev.*, **118**, 1483–1506, [https://doi.org/10.1175/1520-0493\(1990\)118<1483:AMFCSW>2.0.CO;2](https://doi.org/10.1175/1520-0493(1990)118<1483:AMFCSW>2.0.CO;2).
- Haertel, P., K. Straub, and A. Budsock, 2015: Transforming circumnavigating Kelvin waves that initiate and dissipate the Madden–Julian Oscillation. *Quart. J. Roy. Meteor. Soc.*, **141**, 1586–1602, <https://doi.org/10.1002/qj.2461>.
- Hogan, E., A. Shelly, and P. Xavier, 2015: The observed and modelled influence of the Madden–Julian Oscillation on East African rainfall. *Meteor. Appl.*, **22**, 459–469, <https://doi.org/10.1002/met.1475>.
- Huang, P., C. Chou, and R. Huang, 2013: The activity of convectively coupled equatorial waves in CMIP3 global climate models. *Theor. Appl. Climatol.*, **112**, 697–711, <https://doi.org/10.1007/s00704-012-0761-4>.
- Huffman, G. J., and Coauthors, 2007: The TRMM Multisatellite Precipitation Analysis: Quasi-global, multiyear, combined sensor precipitation estimates at fine scales. *J. Hydrometeorol.*, **8**, 38–55, <https://doi.org/10.1175/JHM560.1>.
- Jackson, B., S. E. Nicholson, and D. Klotter, 2009: Mesoscale convective systems over western equatorial Africa and their relationship to large-scale circulation. *Mon. Wea. Rev.*, **137**, 1272–1294, <https://doi.org/10.1175/2008MWR2525.1>.
- Janicot, S., F. Mounier, N. M. J. Hall, S. Leroux, B. Sultan, and G. N. Kiladis, 2009: Dynamics of the West African monsoon. Part IV: Analysis of 25–90-day variability of convection and the role of the Indian monsoon. *J. Climate*, **22**, 1541–1564, <https://doi.org/10.1175/2008JCLI2314.1>.
- , —, B. Sultan, and G. N. Kiladis, 2010: The dynamics of the West African monsoon. Part V: The detection and role of the dominant modes of convectively coupled equatorial Rossby waves. *J. Climate*, **23**, 4005–4024, <https://doi.org/10.1175/2010JCLI3221.1>.
- Janiga, M. A., C. J. Schreck III, J. A. Ridout, M. Flatau, N. P. Barton, E. J. Metzger, and C. A. Reynolds, 2018: Subseasonal forecasts of convectively coupled equatorial waves and the MJO: Activity and predictive skill. *Mon. Wea. Rev.*, **146**, 2337–2360, <https://doi.org/10.1175/MWR-D-17-0261.1>.
- Kamsu-Tamo, P. H., S. Janicot, D. Monkam, and A. Lenouo, 2014: Convection activity over the Guinean coast and Central Africa during northern spring from synoptic to intra-seasonal timescales. *Climate Dyn.*, **43**, 3377–3401, <https://doi.org/10.1007/s00382-014-2111-y>.
- Kendon, E. J., R. A. Stratton, S. Tucker, J. H. Marsham, S. Berthou, D. P. Rowell, and C. A. Senior, 2019: Enhanced future changes in wet and dry extremes over Africa at convection-permitting scale. *Nat. Commun.*, **10**, 1794, <https://doi.org/10.1038/S41467-019-09776-9>.
- Kiladis, G. N., M. C. Wheeler, P. T. Haertel, K. H. Straub, and P. E. Roundy, 2009: Convectively coupled equatorial waves. *Rev. Geophys.*, **47**, RG2003, <https://doi.org/10.1029/2008RG000266>.
- Lafore, J.-P., and Coauthors, 2017: A multi-scale analysis of the extreme rain event of Ouagadougou in 2009. *Quart. J. Roy. Meteor. Soc.*, **143**, 3094–3109, <https://doi.org/10.1002/qj.3165>.
- Laing, A. G., R. E. Carbone, and V. Levizziani, 2011: Cycles and propagation of deep convection over equatorial Africa. *Mon. Wea. Rev.*, **139**, 2832–2853, <https://doi.org/10.1175/2011MWR3500.1>.

- Liebmann, B., and C. A. Smith, 1996: Description of a complete (interpolated) outgoing longwave radiation dataset. *Bull. Amer. Meteor. Soc.*, **77**, 1275–1277, <https://doi.org/10.1175/1520-0477-77.6.1274>.
- , G. N. Kiladis, L. M. V. Carvalho, C. Jones, C. S. Vera, I. Blade, and D. Allured, 2009: Origin of convectively coupled Kelvin waves over South America. *J. Climate*, **22**, 300–315, <https://doi.org/10.1175/2008JCLI2340.1>.
- Lock, A. P., A. R. Brown, M. R. Bush, G. M. Martin, and R. N. B. Smith, 2000: A new boundary layer mixing scheme. Part I: Scheme description and single-column model tests. *Mon. Wea. Rev.*, **128**, 3187–3199, [https://doi.org/10.1175/1520-0493\(2000\)128<3187:ANBLMS>2.0.CO;2](https://doi.org/10.1175/1520-0493(2000)128<3187:ANBLMS>2.0.CO;2).
- Matsuno, T., 1966: Quasi-geostrophic motions in the equatorial area. *J. Meteor. Soc. Japan*, **44**, 25–43, https://doi.org/10.2151/jmsj1965.44.1_25.
- Matthews, A. J., 2008: Primary and successive events in the Madden–Julian oscillation. *Quart. J. Roy. Meteor. Soc.*, **134**, 439–453, <https://doi.org/10.1002/qj.224>.
- McCrary, R. R., D. A. Randall, and C. Stan, 2014: Simulations of the West African monsoon with a superparameterized climate model. Part I: The seasonal cycle. *J. Climate*, **27**, 8303–8322, <https://doi.org/10.1175/JCLI-D-13-00676.1>.
- Mekonnen, A., and C. D. Thorncroft, 2016: On mechanisms that determine synoptic time scale convection over East Africa. *Int. J. Climatol.*, **36**, 4045–4057, <https://doi.org/10.1002/joc.4614>.
- , —, and A. R. Aiyyer, 2006: Analysis of convection and its association with African easterly waves. *J. Climate*, **19**, 5405–5421, <https://doi.org/10.1175/JCLI3920.1>.
- , —, —, and G. N. Kiladis, 2008: Convectively coupled Kelvin waves over tropical Africa during the boreal summer: Structure and variability. *J. Climate*, **21**, 6649–6667, <https://doi.org/10.1175/2008JCLI2008.1>.
- Mera, R., A. G. Laing, and F. Semazzi, 2014: Moisture variability and multiscale interactions during spring in West Africa. *Mon. Wea. Rev.*, **142**, 3178–3198, <https://doi.org/10.1175/MWR-D-13-00175.1>.
- Mounier, F., G. N. Kiladis, and S. Janicot, 2007: Analysis of the dominant mode of convectively coupled Kelvin waves in the west African monsoon. *J. Climate*, **20**, 1487–1503, <https://doi.org/10.1175/JCLI4059.1>.
- Nakazawa, T., 1988: Tropical super clusters within intraseasonal variations over the western Pacific. *J. Meteor. Soc. Japan*, **66**, 823–839, https://doi.org/10.2151/jmsj1965.66.6_823.
- NASA, 2015: Tropical Rainfall Measuring Mission brightness temperature and 3B42 precipitation product, version 7. NASA Goddard Earth Sciences Data and Information Service Center, accessed 28 August 2014, http://disc.sci.gsfc.nasa.gov/precipitation/documentation/TRMM_README/TRMM_3B42_readme.shtml.
- Nesbitt, S. W., R. Cifelli, and S. A. Rutledge, 2006: Storm morphology and rainfall characteristics of TRMM precipitation features. *Mon. Wea. Rev.*, **134**, 2702–2721, <https://doi.org/10.1175/MWR3200.1>.
- Nguyen, H., and J.-P. Duvel, 2008: Synoptic wave perturbations and convective systems over equatorial Africa. *J. Climate*, **21**, 6372–6388, <https://doi.org/10.1175/2008JCLI2409.1>.
- Niang, I., O. C. Ruppel, M. A. Abdrabo, A. Essel, C. Lennard, J. Padgham, and P. Urquhart, 2014: Africa. *Climate Change 2014: Impacts, Adaptation, and Vulnerability. Part B: Regional Aspects*, V. R. Barros, et al., Eds., Cambridge University Press, 1199–1265.
- Nicholson, S. E., 2013: The West African Sahel: A review of recent studies on the rainfall regime and its interannual variability. *ISRN Meteor.*, **2013**, 453521, <https://doi.org/10.1155/2013/453521>.
- , 2017: Climate and climatic variability of rainfall over eastern Africa. *Rev. Geophys.*, **55**, 590–635, <https://doi.org/10.1002/2016RG000544>.
- , 2018: The ITCZ and the seasonal cycle over equatorial Africa. *Bull. Amer. Meteor. Soc.*, **99**, 337–348, <https://doi.org/10.1175/BAMS-D-16-0287.1>.
- , and J. P. Grist, 2003: The seasonal evolution of the atmospheric circulation over West Africa and equatorial Africa. *J. Climate*, **16**, 1013–1030, [https://doi.org/10.1175/1520-0442\(2003\)016<1013:TSEOTA>2.0.CO;2](https://doi.org/10.1175/1520-0442(2003)016<1013:TSEOTA>2.0.CO;2).
- NOAA, 2018: Interpolated outgoing longwave radiation. Physical Sciences Division of NOAA/OAR/ESRL, accessed 16 May 2018, https://www.esrl.noaa.gov/psd/data/gridded/data.interp_OLR.html.
- Prein, A. F., and Coauthors, 2015: A review on regional convection-permitting climate modeling: Demonstrations, prospects, and challenges. *Rev. Geophys.*, **53**, 323–361, <https://doi.org/10.1002/2014RG000475>.
- Reynolds, R. W., T. M. Smith, C. Liu, D. B. Chelton, K. S. Casey, and M. G. Schlax, 2007: Daily high-resolution-blended analyses for sea surface temperature. *J. Climate*, **20**, 5473–5496, <https://doi.org/10.1175/2007JCLI1824.1>.
- Roundy, P. E., 2012: Observed structure of convectively coupled waves as a function of equivalent depth: Kelvin waves and the Madden–Julian oscillation. *J. Atmos. Sci.*, **69**, 2097–2106, <https://doi.org/10.1175/JAS-D-12-03.1>.
- , 2014: Regression analysis of zonally narrow components of the MJO. *J. Atmos. Sci.*, **71**, 4253–4275, <https://doi.org/10.1175/JAS-D-13-0288.1>.
- , and W. M. Frank, 2004: A climatology of waves in the equatorial region. *J. Atmos. Sci.*, **61**, 2105–2132, [https://doi.org/10.1175/1520-0469\(2004\)061<2105:ACOWIT>2.0.CO;2](https://doi.org/10.1175/1520-0469(2004)061<2105:ACOWIT>2.0.CO;2).
- Sandjon, A. T., A. Nzeukou, C. Tchawoua, and T. Siddi, 2014: On the differences in the intraseasonal rainfall variability between western and eastern central Africa: Case of 10–25-day oscillations. *J. Climatol.*, **2014**, 434960, <https://doi.org/10.1155/2014/434960>.
- Schlueter, A., A. H. Fink, P. Knippertz, and P. Vogel, 2019a: A systematic comparison of tropical waves over northern Africa. Part I: Influence on rainfall. *J. Climate*, **32**, 1501–1523, <https://doi.org/10.1175/JCLI-D-18-0173.1>.
- , —, and —, 2019b: A systematic comparison of tropical waves over northern Africa. Part II: Dynamics and thermodynamics. *J. Climate*, **32**, 2605–2625, <https://doi.org/10.1175/JCLI-D-18-0651.1>.
- Sinclair, Z., A. Lenouo, C. Tchawoua, and S. Janicot, 2015: Synoptic Kelvin type perturbation waves over Congo basin over the period 1979–2010. *J. Atmos. Sol. Terr. Phys.*, **130–131**, 43–56, <https://doi.org/10.1016/j.jastp.2015.04.015>.
- Smith, R. N. B., 1990: A scheme for predicting layer clouds and their water content in a general circulation model. *Quart. J. Roy. Meteor. Soc.*, **116**, 435–460, <https://doi.org/10.1002/qj.49711649210>.
- Stratton, R., and Coauthors, 2018: A pan-Africa convection-permitting regional climate simulation with the Met Office Unified Model: CP4-Africa. *J. Climate*, **31**, 3485–3508, <https://doi.org/10.1175/JCLI-D-17-0503.1>.
- Straub, K. H., and G. N. Kiladis, 2003a: Extratropical forcing of convectively coupled Kelvin waves during austral winter. *J. Atmos. Sci.*, **60**, 526–543, [https://doi.org/10.1175/1520-0469\(2003\)060<0526:EFOCCK>2.0.CO;2](https://doi.org/10.1175/1520-0469(2003)060<0526:EFOCCK>2.0.CO;2).

- , and —, 2003b: The observed structure of convectively coupled Kelvin waves: Comparison with simple models of coupled wave instability. *J. Atmos. Sci.*, **60**, 1655–1668, [https://doi.org/10.1175/1520-0469\(2003\)060<1655:TOSOCC>2.0.CO;2](https://doi.org/10.1175/1520-0469(2003)060<1655:TOSOCC>2.0.CO;2).
- , P. T. Haertel, and G. N. Kiladis, 2010: An analysis of convectively coupled Kelvin waves in 20 WCRP CMIP3 global coupled climate models. *J. Climate*, **23**, 3031–3056, <https://doi.org/10.1175/2009JCLI3422.1>.
- Taylor, C. M., and Coauthors, 2017: Frequency of extreme Sahelian storms tripled since 1982 in satellite observations. *Nature*, **544**, 475–478, <https://doi.org/10.1038/NATURE22069>.
- Tompkins, A., A. Diongue-Niang, D. J. Parker, and C. D. Thorncroft, 2005: The African easterly jet in the ECMWF Integrated Forecast System: 4D-Var analysis. *Quart. J. Roy. Meteor. Soc.*, **131**, 2861–2885, <https://doi.org/10.1256/qj.04.136>.
- Walters, D. N., and Coauthors, 2017: The Met Office Unified Model global atmosphere 6.0/6.1 and JULES Global land 6.0/6.1 configurations. *Geosci. Model Dev.*, **10**, 1487–1520, <https://doi.org/10.5194/gmd-10-1487-2017>.
- , and Coauthors, 2019: The Met Office Unified Model Global Atmosphere 7.0/7.1 and JULES Global Land 7.0 configurations. *Geosci. Model Dev.*, **12**, 1909–1963, <https://doi.org/10.5194/gmd-12-1909-2019>.
- Wang, H., and R. Fu, 2007: The influence of Amazon rainfall on the Atlantic ITCZ through convectively coupled Kelvin waves. *J. Climate*, **20**, 1188–1201, <https://doi.org/10.1175/JCLI4061.1>.
- Wang, L., and T. Li, 2017: Convectively coupled Kelvin waves in CMIP5 coupled climate models. *Climate Dyn.*, **48**, 767–781, <https://doi.org/10.1007/s00382-016-3109-4>.
- Washington, R., R. James, H. Pearce, W. M. Pokam, and W. Moufouma-Okia, 2013: Congo basin rainfall climatology: Can we believe the climate models? *Philos. Trans. Roy. Soc. London*, **368B**, 20120296, <https://doi.org/10.1098/rstb.2012.0296>.
- Wheeler, M., and G. N. Kiladis, 1999: Convectively coupled equatorial waves: Analysis of clouds and temperature in the wavenumber–frequency domain. *J. Atmos. Sci.*, **56**, 374–399, [https://doi.org/10.1175/1520-0469\(1999\)056<0374:CCEWAO>2.0.CO;2](https://doi.org/10.1175/1520-0469(1999)056<0374:CCEWAO>2.0.CO;2).
- Wilson, D. R., A. C. Bushell, A. M. Kerr-Munslow, J. D. Price, and C. J. Morcrette, 2008: PC2: A prognostic cloud fraction and condensation scheme. I: Scheme description. *Quart. J. Roy. Meteor. Soc.*, **134**, 2093–2107, <https://doi.org/10.1002/qj.333>.
- Wood, N., and Coauthors, 2014: An inherently mass-conserving semi-implicit semi-Lagrangian discretization of the deep-atmosphere global non-hydrostatic equations. *Quart. J. Roy. Meteor. Soc.*, **140**, 1505–1520, <https://doi.org/10.1002/qj.2235>.
- Yang, G.-Y., B. Hoskins, and J. Slingo, 2007: Convectively coupled equatorial waves. Part III: Synthesis structures and their forcing and evolution. *J. Atmos. Sci.*, **64**, 3438–3451, <https://doi.org/10.1175/JAS4019.1>.
- Zipser, E. J., D. J. Cecil, C. Liu, S. W. Nesbitt, and D. P. Yorty, 2006: Where are the most intense thunderstorms on Earth? *Bull. Amer. Meteor. Soc.*, **87**, 1057–1071, <https://doi.org/10.1175/BAMS-87-8-1057>.